PHYSICAL MODELING OF SOLID SPHERES' MOTION UNDER SOLITARY WAVE ATTACK

A THESIS SUBMITTED TO
THE GRADUATE SCHOOL OF NATURAL AND APPLIED SCIENCES
OF
MIDDLE EAST TECHNICAL UNIVERSITY

BY

KORAY DENİZ GÖRAL

IN PARTIAL FULFILLMENT OF THE REQUIREMENTS
FOR
THE DEGREE OF MASTER OF SCIENCE
IN
CIVIL ENGINEERING

AUGUST 2020

Approval of the thesis:

AN EXPERIMENTAL STUDY ON THE MOTION OF SOLID SPHERES UNDER SOLITARY WAVE ATTACK

submitted by **KORAY DENİZ GÖRAL** in partial fulfillment of the requirements for the degree of **Master of Science** i**n Civil Engineering, Middle East Technical University** by,

Prof. Dr. Halil Kalıpçılar
Dean, Graduate School of **Natural and Applied Sciences**

Prof. Dr. Ahmet Türer
Head of the Department, **Civil Engineering**

Assist. Prof. Dr. Cüneyt Baykal
Supervisor, **Civil Engineering, METU**

Prof. Dr. Ahmet Cevdet Yalçıner
Co-Supervisor, **Civil Engineering, METU**

Examining Committee Members:

Prof. Dr. İsmail Yücel
Civil Engineering, METU

Assist. Prof. Dr. Cüneyt Baykal
Civil Engineering, METU

Prof. Dr. Ahmet Cevdet Yalçıner
Civil Engineering, METU

Assoc. Prof. Dr. Kubilay Cihan
Civil Engineering, Kırıkkale University

Assist. Prof. Dr. Gülizar Özyurt Tarakcıoğlu
Civil Engineering, METU

Date: 31.08.2020

I hereby declare that all information in this document has been obtained and presented in accordance with academic rules and ethical conduct. I also declare that, as required by these rules and conduct, I have fully cited and referenced all material and results that are not original to this work.

Name, Last name: Koray Deniz Göral

Signature:

ABSTRACT

PHYSICAL MODELING OF SOLID SPHERES’ MOTION UNDER SOLITARY WAVE ATTACK

Göral, Koray Deniz
Master of Science, Civil Engineering
Supervisor: Assist. Prof. Dr. Cüneyt Baykal
Co-Supervisor: Prof. Dr. Ahmet Cevdet Yalçıner

August 2020, 67 pages

In this study, the motion and collision of the spheres under the solitary wave attack is studied. The physical experiments were carried out in a wave channel at Middle East Technical University Ocean Engineering Research Center Laboratory that has 26 m length and 0.9 m width with the slopes of 1:20 for breaking solitary wave conditions and 1:4.5 for non-breaking solitary wave conditions that followed by a horizontal area. Two different colored spherical homogeneous balls with a diameter of 10 cm and 2712 kg/m^3 in density are used for the single sphere and double sphere experiments. The motion of a single sphere and the motion and the collision of the double sphere cases were examined with the changing permeability of the bottom as impermeable and porous, water levels and type of solitary waves as non-breaking and breaking. Therefore, 4 different experimental configurations were constructed and 16 different cases were performed in the present study. Each case was repeated 21 times to reduce the bias on the results. The paths of the spheres were tracked with the homemade image processing code based on color detection algorithm. The dimensionless trajectories and the dimensionless velocities are given for each case. It is seen from the results that different permeabilities of the bottom, water levels and types of the solitary waves are significantly affecting the behavior of the motion of the spheres. Also, the collision of the spheres is considerably changing the behavior of the motion of the spheres, especially when they did not collide in the half-submerged condition effected with the breaking solitary waves. This study presents a unique dataset that shows the fundamentals of the motion of the spheres under a solitary wave attack. Besides, the mentioned dataset can be used for the calibration and validation purposes of the newly developed CFD-DEM solvers.

Keywords: Motion and collision of solid spheres, solitary wave, wave force, color tracking

ÖZ

SOLİTER DALGA ETKİSİ ALTINDAKİ KÜRELERİN HAREKETİ'NİN FİZİKSEL MODELLENMESİ

Göral, Koray Deniz
Yüksek Lisans, İnşaat Mühendisliği
Tez Yöneticisi: Asist. Prof. Dr. Cüneyt Baykal
Ortak Tez Yöneticisi: Prof. Dr. Ahmet Cevdet Yalçıner

Ağustos 2020, 67 sayfa

Bu fiziksel deney çalışmasında soliter dalga etkisi altındaki kürelerin hareketleri laboratuvar ortamında incelenmiştir. Fiziksel deneyler için Orta Doğu Teknik Üniversitesi Kıyı ve Deniz Laboratuvarında 26 m uzunluğunda ve 0,9 m genişliğinde kırılan soliter dalgalar için 1:20 ve kırılmayan soliter dalgalar için 1:4,5 oranlarında eğime ve sonrasında düz bir alana sahip dalga kanalı inşa edilmiştir. İki farklı renge boyanmış 10 cm çapında ve 2712 kg/m^3 ağırlığındaki homojen küreler tek küre ve çift küre deneylerinde kullanılmıştır. Değiştirilen yüzey geçirgenlik oranının (geçirgen olmayan ya da geçirgen olan), su seviyesinin ve soliter dalga tipinin (kırılmayan ya da kırılan) küreler üzerinde yarattığı etki, tek toplu deneylerde topların hareketi, çift toplu deneylerde ise topların hareketinin yanı sıra çarpışma davranışlarına etkisi incelenmiştir. Bu değişkenler göz önüne alınarak 4 farklı deneysel kurulum oluşturulmuştur. Fiziksel deney setine bakıldığında yapılan deneylerle 16 farklı durum çalışılmıştır. Her bir durum 21 kere tekrarlanmış ve bu sayede sonuçlar üzerinde oluşabilecek hatalar en aza indirilmeye çalışılmıştır. Deneylerde kullanılan kürelerin soliter dalga etkisi altında izlediği yollar renk izleme metodu ile oluşturulan görüntü izleme koduyla takip edilmiştir. Kürelerin boyutsuz yörüngeleri ve boyutsuz hızları her bir durum için verilmiştir. Deney sonuçlarına bakıldığında değişen zemin geçirgenliği, su seviyesi ve soliter dalga tipinin kürelerin hareketlerini önemli ölçüde etkilediği görüşmüştür. Buna ek olarak, kürelerin birbiri ile çarpışması durumu kürelerin hareketini önemli ölçüde etkilemektedir. Bu çarpışma etkisi kürelerin yarı suya batık halde kırılan soliter dalga etkisi altında çarpışmadan izledikleri hareketlerine bakılarak anlaşılabilir. Soliter dalga etkisi altında hareket eden kürelerin temel özelliklerinin paylaşıldığı bu deneyler literatüre benzersiz bir veri seti sağlamıştır. Ayrıca sağlanan veri seti ile günümüzde yeni yeni popülerleşen CFD-DEM çözücülerinin kalibrasyonu ve sonuçlarının doğrulanması yapılabilir.

Anahtar Kelimeler: Kürelerin hareketi ve çarpışması, soliter dalga, dalga kuvveti, renk izleme

Dedicated to my beautiful family and beloved ones…

ACKNOWLEDGMENTS

I would like to express my deepest gratitude to my supervisor Assist. Prof. Dr. Cüneyt Baykal and co-supervisor Prof. Dr. Ahmet Cevdet Yalçıner for their guidance, advice, criticism, encouragements and insight throughout this research. Many good things in my life have happened thanks to you in that small amount of time, and I will always appreciate you giving me the chance to create those great memories. I will always feel privileged thanks to your efforts on me.

I would like to express my most sincere gratitude to Dr. Hasan Gökhan Güler. We worked together on the entire research, and I appreciate his guidance as well as his patience towards me. Thanks to his effort on me, I learned a lot from my mistakes, and I went one step forward thanks to his massive amount of advice throughout my master’s study. Throughout my master’s research, we laughed a lot, worked a lot, and shared a lot. Therefore, I have to thank him also for all the happy and fruitful memories we created together.

I would like to thank Prof. Dr. Ayşen Ergin for her cheerful perspective as well as the enlightening knowledge that she has on coastal engineering. She is the most valuable one for the coastal engineering family, and I am very lucky to be her student and got her perspective towards life.

I would like to thank Assist. Prof. Dr. Gülizar Özyurt Tarakcıoğlu and Dr. Işıkhan Güler for sharing their knowledge and experience with me through my master’s study. They enlightened my path with their knowledge, and I see things from a different perspective thanks to their guidance.

I would like to thank intern Roman Arris Tijsseling for his supports in the experimental stage and the laboratory technicians Yusuf Korkut and Eyüp Uğur for their effort in creating the experimental setups.

I would like to thank my dearest friends who are part of the coastal engineering family Mehmet Sedat Gözlet, Cem Bingöl, Can Özsoy, Barış Ufuk Şentürk, Ghazal Khodkar and Kadir Karakaş who supported me and shared great moments with me.

I would like to thank all my friends in coastal engineering family Emre Yıldırım, Batuhan Çandır, Aslıhan Devran, Bora Yalçıner, Gözde Güney Doğan, Gizem Ezgi Çınar, Emrecan Işık, Utku Uzun, İlker Çoban, Mert Yaman, Berkay Akyol and Yağız Arda Çiçek for their presence in my life and all the memories that we shared.

I would like to thank my dearest life companions Batuhan Şahin, Mustafa Efekan Çevik and Kamer Büşra Aydos for their limitless friendship and support throughout my life.

Finally, I would like to express my most sincere gratitude to my family. I would like to thank my mother Hülya Göral, my father Metin Göral and my little sister Umut Zeynep Göral for their endless support to fulfill my life goals. I am very lucky to have my family, and I never change a bit of tiny memory that I stored in my life with them.

This research is supported by the Scientific and Technological Research Council of Turkey (TUBITAK, Grant No: 217M722).

TABLE OF CONTENTS

CHAPTERS

LIST OF TABLES

TABLES

LIST OF FIGURES

FIGURES

LIST OF ABBREVIATIONS

ABBREVIATIONS

SP	Sphere
NB	Non-Breaking Solitary Wave
B	Breaking Solitary Wave
S	Single Unit
T	Two Units
D	Dry
H	Half-Water
I	Impermeable Base
P	Porous Base
WG	Wave Gauge
ADV	Acoustic Doppler Velocimeter
FFT	Fast Fourier Transform
M	Mass
L	Length
T	Time

LIST OF SYMBOLS

SYMBOLS	
n	Number of Selected Experiments
μ	Mean
σ	Standard Deviation
α	Significance Level
δ	Non-centrality Parameter
β	Power of T-Test
G	Non-Central T-Distribution
ζ	Wave Paddle Trajectory
h_{water}	Still Water Depth
η_{wave}	Wave Profile
k_{decay}	Outskirt Decay Coefficient
c	Wave Celerity
ρ	Specific Weight of Water
g	Gravitational Force
x	Longitudinal Dimension
y	Transverse Dimension
t	Time
h	Water Depth
ρ_s	Density of the Sphere

D	Diameter of the Sphere
H	Solitary Wave Height
X	Longitudinal Displacement
Y	Transverse Displacement
$V_{s,x}$	Longitudinal Velocity
X_c	Distance Between the Center of the Spheres

CHAPTER 1

INTRODUCTION

The motion of the particles is a major research area that is vastly studied throughout history. There are so many examples of natural phenomena and engineering problems related to the mentioned topic. The debris motion driven by the tsunami or storm surge is gained attention by the coastal and ocean researchers in the last 20 years. Therefore, these researchers carried out experiments to understand the physics under the motion of the particles on the area of the coastal and ocean engineering. The findings from these studies put more value on the knowledge of the hydrodynamic forces acting on the structures, and this helped coastal engineers to design more durable coastal structures like rubble mound breakwaters. However, most of the studies related to this research area were examined the motion of the prismatic particles, and the studies considering the motion of the spherical particles were only examined the motion in the stationary fluids in different contexts such as oil, glycerin and water. Therefore, there is a need for researches considering the motion of the spherical particles moving in the non-stationary fluids.

In the present study, the motion and collision of solid spheres under solitary wave attack are experimentally investigated in a wave channel. A sloping bottom followed by a horizontal area was constructed inside of this wave channel and used as an experimental area. The non-breaking and breaking solitary waves were created by the two different slopes, and the motion of a single sphere and the motion and collision of two spheres were investigated along the horizontal area. The permeability of the horizontal area was changed to alternate the flow characteristics around the spheres. Also, two different water levels were used in the experiments for investigating the behavior of the spheres with the changing water levels. In total, 16 different experimental cases on 4 different experimental configurations were studied.

This study is primarily aimed to present the fundamentals of the motion and collision of the spherical particles under a solitary wave attack on a horizontal region for various experimental conditions. Therefore, the physics behind the motion of the spheres under the attack of the solitary wave was examined in detail. Also, the coastal and ocean engineering studies can get an advantage from the findings of the presented research by considering the experimental results to understand how the hydrodynamic forces drive the spherical particles, which can help engineers to design the marine structures better. Furthermore, the dataset created by the results of these experiments is very advantageous for the newly being developed computational fluid dynamics-discrete element method (CFD-DEM) solvers that can also be used in the future designs of the marine structures. These CFD-DEM solvers can show very detailed hydrodynamic forces acting on the coastal structure in the future. However, these numerical solvers are newly developing, and the trials with the primary geometrical particles are needed for the very first steps of the calibration and validation of these solvers. For example, considering the rubble mounds in the rubble mound breakwaters as the ideal spheres for the very first step through the complex rubble mound structure, the presented experimental dataset can add excellent value to the calibration and validation of the newly developed numerical models solving debris motion driven by the extreme hydrodynamic forces. It can be noted that the experimental dataset presented in this study is a unique integrated dataset on the motion and collision of the spherical particles under a solitary wave attack as there is no available dataset in the literature focusing on this research topic. The experimental dataset is available upon request.

This project is supported by The Scientific and Technological Research Council of Turkey (TUBITAK) under the project name “Modeling the Motion of Units Forming Rubble Mound Coastal Protection Structures under Wave Attack using Immersed Boundary and Discrete Element Numerical Methods” and project number “217M722”. This TUBITAK project was supervised by Prof. Dr. Ahmet Cevdet Yalçıner between the project dates “01/05/2018 – 01/05/2020”.

This study structured as follows:

In Chapter 2, “Literature Review”, the researches related to the present study are introduced briefly.

In Chapter 3, “Experimental Setup and Analysis”, firstly the experimental cases and the related conditions are introduced in detail. Then, the structural parameters of the 4 different experimental setups with the related cases are given, and the instrumentations for the measuring of the experimental data are presented. Later, the solitary wave generation is explained. Finally, the analysis protocol of the motion of the spheres with the dimensionless analysis chapter is presented in detail.

In Chapter 4, “Results”, firstly the water surface elevations are given for the two different water levels, and the results are compared for each wave gauge location. Then, the water particle velocity measurements are presented and compared for the different water levels. Finally, all of the experimental results of the 16 different cases are given with the dimensionless trajectory and dimensionless velocity graphs, in detail.

In Chapter 5, “Discussion of the Results”, the results of the experimental cases are discussed into 4 main subsections to clarify the fundamentals of the motion of the spheres under solitary wave attack.

In Chapter 6, “Conclusions”, the major conclusions and the recommendations of the present study are given briefly.

CHAPTER 2

LITERATURE REVIEW

The number and variety of researches considering the motion of the particles are increased throughout the years, especially in the last 20 years. However, the researches considering the motion of the spherical particles driven by the hydrodynamic forces are not yet studied well, and there is almost no research on the related topic. Therefore, in this section, the interrelated studies on the presented research area are given firstly considering the motion on the stationary fluids. Later, the studies considering the problems on the coastal engineering are given in detail. The methodologies used in the mentioned researches are introduced briefly.

The motion and the collusion of the spherical particles were mostly investigated in stationary fluids such as water, oil and glycerin. Joseph et al. (2001) examined the trajectories of spherical particles made from different materials like glass, steel and nylon. The spherical particles were submerged into various stationary fluids, which were prepared with a different percentage of the mixture of glycerol with water. The spherical particles were first hanged with an initial angle then released from that position, and the trajectories of the spherical particles were observed one-by-one until they collided with the installed vertical wall inside of the stationary fluid. Gondret et al. (2002) examined the bouncing trajectories of the different spherical particles made from various materials such as tungsten, steel, glass and Teflon. The spherical particles were set loose inside of the stationary fluids like air, water and silicone oil, and their trajectories before and after the collision with the horizontal bottom wall were examined. Pitois et al. (2000) examined the capillary and viscous forces between the two spherical particles. The faces between the two spheres were wetted with different types of oils. Then, the spheres were separated slowly, and the viscous and capillary forces created by the liquid between the spheres were examined. But, as can be seen from the studies mentioned above, the motion and collision of the spherical particles were mostly studied with small spherical particles that were inside of the stationary fluids, and the motion was controlled mainly by the gravitational forces.

In coastal and ocean engineering, the structures constructed inside or near the sea or ocean are generally prone to withstand different kinds of hydrodynamic forces such as cyclic or extreme wave forces. Therefore, the debris motion under the influence of the extreme hydrodynamic conditions such as tsunami and storm surges are widely studied. Rueben et al. (2015) examined the debris motion under the tsunami attack. Rectangular boxes are selected as debris specimens. These boxes were placed on a concrete basin, which was constructed as an unobstructed beach. The motion of the rectangular boxes under the attack of the tsunami was recorded with two video cameras placed on the top of the experimental area. With the optical tracking method, the centroid position, velocity, angle and rate of rotation measurements of the rectangular boxes were gathered. Shafiei et al. (2016) extended the studies on tsunami-borne debris motion by measuring the impact acceleration forces between the debris and inland structures with the technique named smart debris approach. Circular disks were used as debris specimens, and the acceleration data was collected with the accelerometer installed inside of these circular disks. Also, with the optical tracking method, the rotation, velocity and acceleration data of the circular disks were collected. Goseberg et al. (2016) extended the smart debris approach using state-of-the-art wireless spatial data recorders, which can work without the need for optical tracking. Rectangular boxes were used as debris specimens. By using the smart debris technique, the position, orientation and inertial forces of single debris under the broken solitary wave attack were measured. The spatial data coming from the motion sensor was validated with the video recordings, and it is seen that smart debris technique is useful for the catching trajectories of objects in flood, tsunami flow or motion of armor stone elements in breakwaters. Later, Nistor et al. (2017) made an extensive search on the debris transport, debris impact, and debris damming with searching nearly all the related literature. Also, numerical modeling of the debris motion was included in the research. It is stated in this research that the number of studies objected to solid-solid/solid-fluid momentum transfer, as well as the factors governing the actual debris entrainment should be increased. Also, it can be seen from the study that the meticulous and high-resolution studies are needed for the detailed calibration and validation of the numerical models considering the debris motion.

Stolle et al. (2016) proposed color-based optical tracking and examined the accuracy of the optical tracking of the debris motion with different evaluation methods. Rectangular boxes represented as scaled containers were used as debris material, and they were moved under the attack of tsunami-like flow over a horizontal bottom. After the evaluations of the optical tracking algorithm, it is seen that the tracking algorithm is accurate for catching the centroid of the objects if the lightning is consistent. Later, Stolle et al. (2017) used the same optical tracking algorithm for the assessment of the risk of rectangular debris loading considering the trajectory of debris under the extreme hydrodynamic conditions like dam-break. With the camera-based object-tracking, the trajectories and the velocities of the debris particles were captured. Stolle et al. (2019) extended the studies on the transportation of the rectangular debris particles under the attack of tsunami-like flow conditions. Besides the optical analysis for the debris spreading, displacement and velocity, the friction effect on the debris motion was also discussed with the friction tests applied on the rectangular debris particles. Although most of the debris materials created by the attack of the extreme hydrodynamic conditions are considered as prismatic structures such as containers, buildings and vehicles, there are also spherical structures considered as debris materials such as the rolled and displaced spherical liquid petroleum gas (LPG) storage tanks near Ichihara, Japan, under the impact of the 2011 Tohoku Earthquake Tsunami (Zama et al., 2012). The displaced spherical LPG storage tanks can be seen in Figure 2.1.

Figure 2.1. Displaced Spherical LPG Storage Tanks (Zama et al., 2012)

The computational fluid dynamics (CFD) applications also study the motion and collision of the spherical particles under the scope of the calibration and validation of the specific CFD solvers. These CFD solvers are generally coupled with particle motion solvers, such as the discrete element method (DEM). To study this issue, Guler et al. (2018) examined a single set of experiments of the motion and collision of the two spheres under solitary wave attack and tried to validate a CFD-DEM solver. Although there are studies like Imamura et al. (2008), which study examined the boulder transport considering scaled cubic or rectangular solid boulders under tsunami attack, this study was the first attempt to create a dataset on the motion and collision of the solid spherical particles involving the solitary wave attack. However, due to the limited number of experiments, there is no generalized discussion on the motion and collision of the spheres. Therefore, it can be seen from the literature review that the studies concerning the motion and the collision of the spherical particles are not studied well, and the number of researches should be increased.

CHAPTER 3

EXPERIMENTAL SETUP AND ANALYSIS

In this section, first, the experimental cases with the repetition analysis are introduced. After that, the experimental setup with the instrumentation, solitary wave generation and the analysis of the experimental data with the dimensionless analysis section are presented in detail.

3.1 Experimental Cases

The experiments were performed using a single sphere and double sphere so that datasets for the motion and the collision of the spheres under the influence of the same conditions were taken separately. A total of 16 different cases were planned throughout the experimental schedule. These cases are manipulated with 4 main conditions; the number of spheres, wave breaking, bottom permeability and water depth. Among these 16 cases, 8 cases were conducted with a single sphere, and 8 cases were conducted with double sphere. Also, considering these 16 cases, 8 cases were performed with the non-breaking solitary waves, while the other 8 cases were performed with the breaking waves. The solitary wave breaking condition was controlled by changing the bottom slope. Also, the permeability of the bottom was changed from impermeable bottom to permeable bottom to understand the effect of the permeability on the motion and the collision of the spheres. In addition, 2 different water levels were used in the experiments, such as; in one case, the spheres are placed on a horizontal dry surface, and in the other case, the spheres are half-submerged on the same horizontal surface. As the presented research is mainly concerned with the region where the sea or ocean is interacting with the rubble mound structure, the experimental setup was planned for representing the motion of dry and half-submerged rubble mounds under the action of the wave forces. The half-submerged condition is named as “half-water” in the experiments. The wave type, the permeability and the water level change are considered as the main parameters of the presented setup, and the experimental cases were created accordingly. All of the 16 cases were repeated 21 times to increase the accuracy of the overall results. The detailed repetition analysis is given in the next section, which is Section 3.1.1.

3.1.1 Repetition Analysis

Although this study investigated the motion of the spherical particles under the attack of the solitary waves, the motion of the cubic particles under the same effect of hydrodynamic conditions and solitary wave attack as spherical particle cases was also investigated as another milestone of the TUBITAK project. It is seen from the initial experimental results that the results of the experiments performed with the cubes showed higher randomness than the results of the experiments with the spheres. Therefore, the reliability of the experiments performed with both spherical and the cubic particles with their results was questioned concerning the number of repetitions that supplied sufficient data to reach an unbiased conclusion for each case. Generally, the number of repeated experiments was randomly selected, which can be seen from the given literature considering the debris experiments, but, in the presented experiments, the number of the repeats for the experimental cases was found with the repeatability analysis. The repetition number for the sphere and cube cases were found with the repeatability experiments performed by the cube experiments as the experiments with the cubes showed higher randomness. Statistical analysis was carried out with a selected cube case performed on the impermeable bottom, which was additionally repeated 100 times to create a dataset for the repeatability analysis. In the repetition analysis, it is believed that the repetition number found from these 100 trials showed the exact result for each case. Below, the repetition analysis taken by the other experimental research is explained in detail.

A two-sided “t-test” was applied with a significance level of 5% using the data of all 100 experiments. The power of the t-test is calculated using Equation 3.1 for changing a number of selected experiments (*n*) assuming that the true mean (μ_1) of the selected *n* experiments from 100 experiments could be at most $\mu_1 = \mu_0 + \sigma_0$ or at least $\mu_1 = \mu_0 - \sigma_0$ where μ_0 is the mean and σ_0 is the standard deviation of these 100 experiments. In Equation 3.1, β is the power of the t-test, and *G* is the non-central t-distribution. *G* is a function of t-distribution with a significance level of α , *(n-1)* degrees of freedom and non-centrality parameter, δ . δ is defined in Equation 3.2. Note that Equation 3.1 is valid when the samples come from a normal distribution (Schloz, 2008). The normality of the sample is checked by the Jarque-Bera test (Jarque, 2011).

$$\beta = G_{n-1,\delta}\left(-t_{n-1}\left(1-\frac{\alpha}{2}\right)\right) + 1 - G_{n-1,\delta}\left(t_{n-1}\left(1-\frac{\alpha}{2}\right)\right) \qquad \text{Eq. (3.1)}$$

$$\delta = \sqrt{n}\frac{\mu_1 - \mu_0}{\sigma_0} \qquad \text{Eq. (3.2)}$$

The power-sample size graph is plotted with a significance level of 5% presented in Figure 3.1. The results of the “t-test” showed that reliable results with a power of 99% could be reached with 21 repetitions.

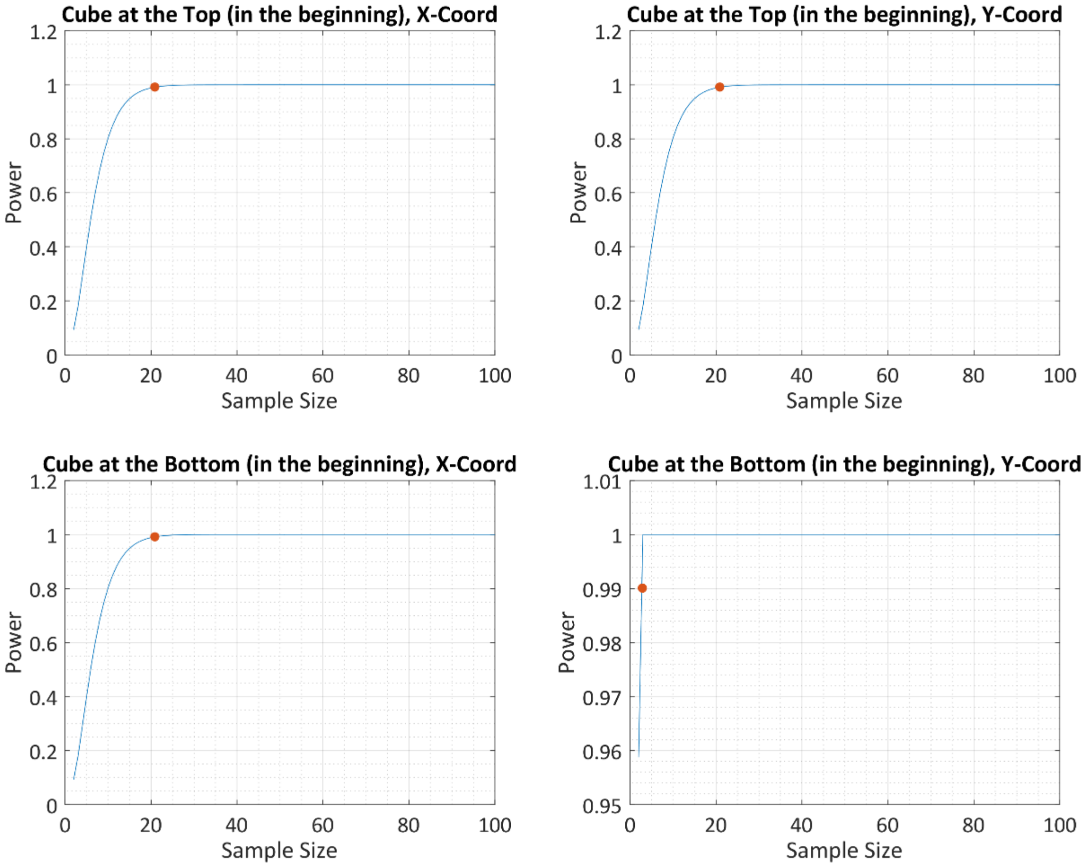

Figure 3.1: Repetition Test Analysis Results

In Table 3.1, the main parameters influencing the behavior of the motion and the collision of the 16 cases, including the unique name tags for each case are summarized. Also, in Figure 3.2, the detailed drawings for the 16 cases are shown to understand better the conditions affecting the motion and the collision of the spheres.

Table 3.1: Description of Experimental Cases

Number and Type of Unit(s)	**Water Level**	**Base**	**Non-Breaking Wave Cases***	**Breaking Wave Cases***
			(Case No)	**(Case No)**
Single Sphere	Dry	Impermeable	SP1-NB-S-DI	SP9-B-S-DI
			(Case 1)	(Case 9)
Single Sphere	Dry	Porous	SP2-NB-S-DP	SP10-B-S-DP
			(Case 2)	(Case 10)
Single Sphere	Half-Water	Impermeable	SP3-NB-S-HI	SP11-B-S-HI
			(Case 3)	(Case 11)
Single Sphere	Half-Water	Porous	SP4-NB-S-HP	SP12-B-S-HP
			(Case 4)	(Case 12)
Double Spheres	Dry	Impermeable	SP5-NB-T-DI	SP13-B-T-DI
			(Case 5)	(Case 13)
Double Spheres	Dry	Porous	SP6-NB-T-DP	SP14-B-T-DP
			(Case 6)	(Case 14)
Double Spheres	Half-Water	Impermeable	SP7-NB-T-HI	SP15-B-T-HI
			(Case 7)	(Case 15)
Double Spheres	Half-Water	Porous	SP8-NB-T-HP	SP16-B-T-HP
			(Case 8)	(Case 16)
***SP: Sphere, NB: Non-Breaking Wave, B: Breaking Wave, S: Single Unit, T: Two-Units, D: Dry, H: Half-Water, I: Impermeable Base, P: Porous Base**				

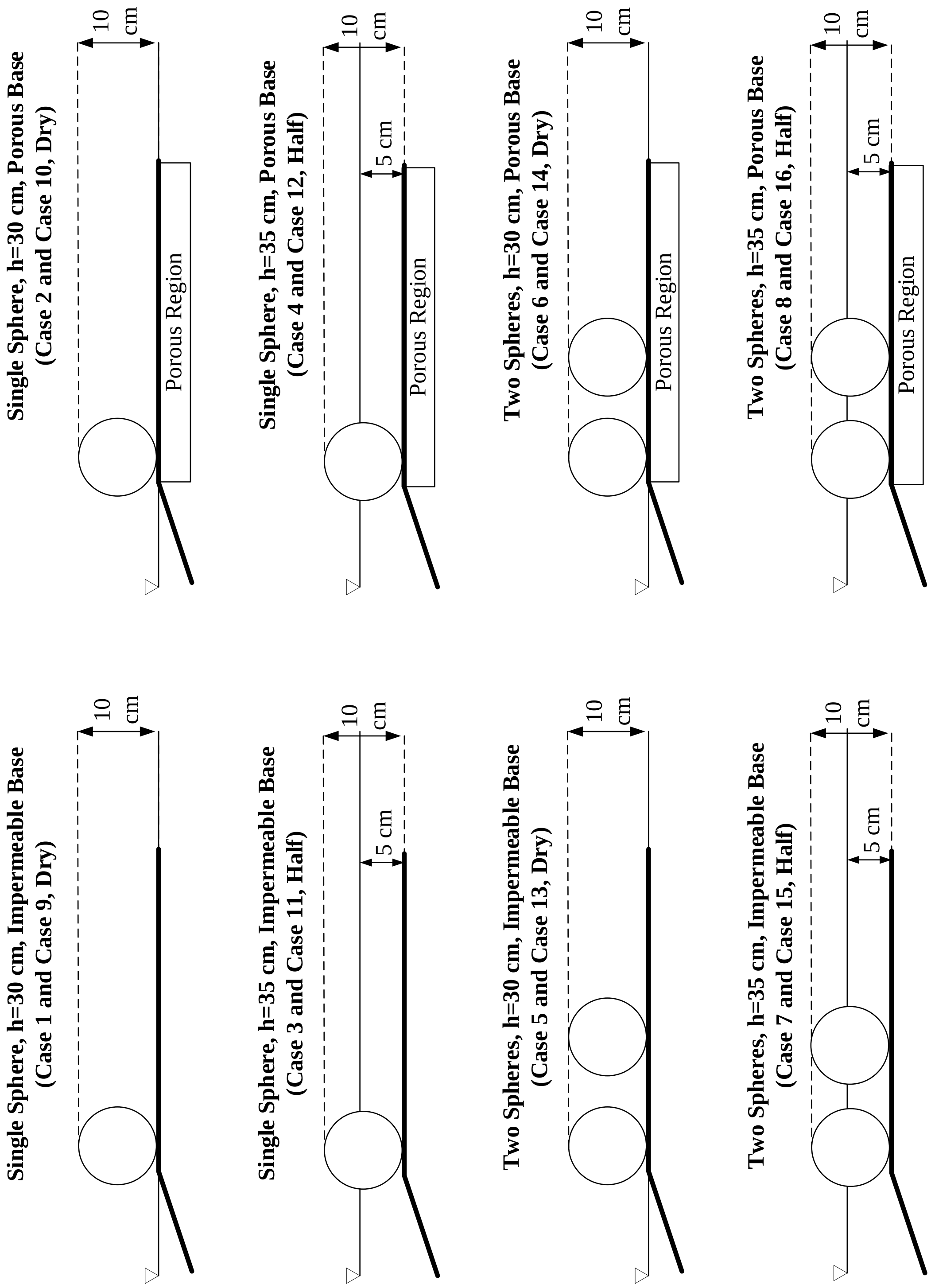

Single Sphere, h=30 cm, Impermeable Base (Case 1 and Case 9, Dry)

Single Sphere, h=30 cm, Porous Base (Case 2 and Case 10, Dry)

Single Sphere, h=35 cm, Impermeable Base (Case 3 and Case 11, Half)

Single Sphere, h=35 cm, Porous Base (Case 4 and Case 12, Half)

Two Spheres, h=30 cm, Impermeable Base (Case 5 and Case 13, Dry)

Two Spheres, h=30 cm, Porous Base (Case 6 and Case 14, Dry)

Two Spheres, h=35 cm, Impermeable Base (Case 7 and Case 15, Half)

Two Spheres, h=35 cm, Porous Base (Case 8 and Case 16, Half)

Figure 3.2: Drawings of the 16 Different Cases with the Related Configurations

3.2 Experimental Setup

The wave flume of the Middle East Technical University Ocean Engineering Research Center Laboratory was used for the experiments. The wave flume that has 26 m in length and 6 m in width was used for the experiments. Inside of the main wave flume, a divided wave channel of 26 m in length and 0.9 m in width was constructed. Inside of this wave channel, a sloping bottom followed by a horizontal area where the spheres are moving and colliding on was built. Two identical spheres were used for the experiments. The spheres were painted as yellow and red, and they are 10 cm in diameter with the same density of 2712 kg/m^3. The density of the spheres was adjusted considering the rubble stone density, which is around 2700 kg/m^3. Also, the diameter of the spheres was selected, considering the developed velocities of the spheres within the given experimental setup. As the sphere diameter increases, the weight of the sphere increases, and under the same solitary wave attack and hydrodynamic conditions, the velocity of the sphere decreases; therefore, by selecting the diameter of the spheres as 10 cm, the velocities of these spheres were developed fully within the limits of the given horizontal area. For the double sphere cases, the sphere located just after the end of the slope considered as the upstream location was named as “Inlet Sphere” and the sphere located far from the inlet sphere towards the downstream section was named as “Outlet Sphere”. Also, the center to center distance between the spheres was selected as 13 cm. This distance was chosen randomly by considering the effect of the solitary wave attack on close spheres. The spheres were located at the horizontal area that had 1.9 m length, 0.9 m width and 0.3 m height. A net was constructed at the end of the horizontal area to stop the spheres going out of the experiment region.

Grilli et al. (1997) inspected the shoaling and the breaking of the solitary waves by examining the solitary wave propagation on the numerous slopes. The results of this research showed that the solitary waves lose their stability and break on slopes milder than 1:4.7. Therefore, the cases with the non-breaking solitary waves were performed with the 1:4.5 slope; on the contrary, the cases with the breaking solitary waves were performed with the 1:20 slope.

The permeability of the bottom was changed with the plywood and rubble stones where the impermeable slope and the impermeable horizontal area were constructed with the plywood while the porous slope and the porous horizontal area were constructed with the rubble stones. Also, it was planned that the porosity of the porous structure has to be built as 0.43. Therefore, before the construction, the porosity of the selected rubblestone mixture was measured with the 10 different test samples taken from the mix of different sized rubble stones. The mean of these porosity tests was found as approximately 0.43, and the porous structure was constructed with the found mixture of the rubble stones. Moreover, a 1 mm thick punched metal sheet with the metal framing was built for the porous cases to eliminate the irregular surface created by the rubble stones and regularize the motion of the spheres moving on the porous horizontal area. Also, the porosity of the punched metal structure was adjusted higher than 0.43 to guarantee that the motion of the spheres was only influenced by the porous rubblestone configuration as the similar application was mentioned in Jensen et al. (2015). The construction phase of the porous bottom can be seen in Figure 3.3.

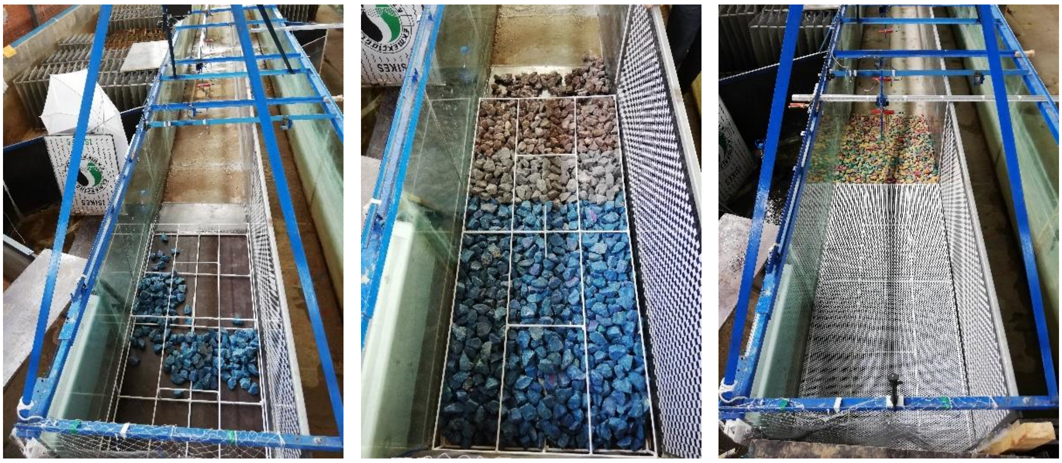

Figure 3.3: Captions for the Construction of the Porous Bottom with 1:4.5 Slope

The water levels were selected considering the initial physical situation of the spheres. The dry condition of the spheres was arranged with the 30 cm water depth in front of the wave generator so that the water level at the horizontal bottom is 0. Also, for simplicity, the 30 cm water depth was named as “Dry” condition for the cases performed with the 30 cm water depth. The half-submerged condition of the spheres was arranged with the 35 cm water depth, as it can be seen that this water depth is calculated by the addition of the radius of the spheres with the height of the horizontal area. Also, for simplicity, the 35 cm water depth was named as “Half-Water” condition for the cases performed with the 35 cm water depth.

3.3 Instrumentation

The solitary waves were created with the piston-type irregular wave generator. The solitary wave input given from the computer was converted to the analog input used by the pistons with the help of a digital servo controller. Moog SmarTEST ONE was used for the digital to analog input data conversation for the piston-type irregular wave generator. The photographs for the digital servo controller and piston-type irregular wave generator are given in Figure 3.4.

(a) (b)

Figure 3.4: Digital Servo Controller (a) and Piston-Type Irregular Wave Generator (b)

The water surface elevations were measured at 5 different points throughout the wave channel. Danish Hydraulic Institute (DHI) Type 202 wave gauges operated at the 40 Hz sampling rate were used at these points to get the recording of the water surface elevations. Also, the water particle velocities were measured with an Acoustic Doppler Velocimeter (ADV) at multiple water depths located at the very first wave gauge location. Nortek Vectrino+ ADV operated at 200 Hz sampling rate was used for the measurement of the water particle velocities. The example photographs for the wave gauge and ADV devices are shown in Figure 3.5.

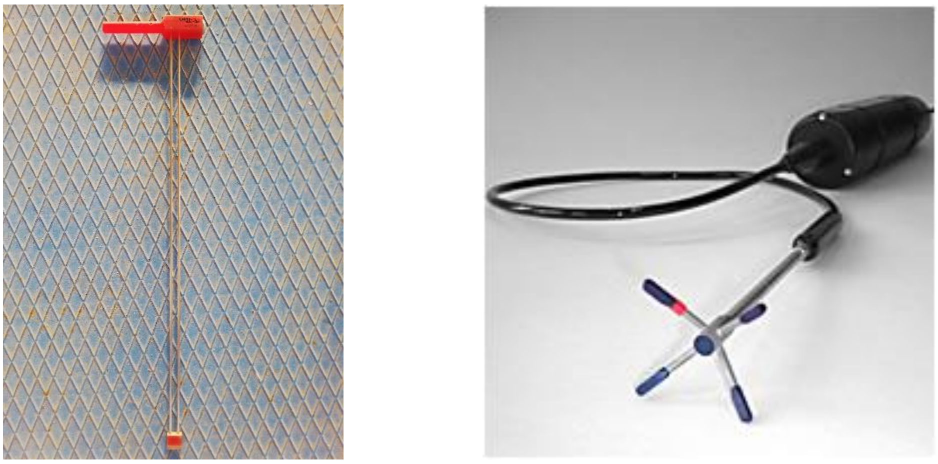

(a) (b)

Figure 3.5: Wave Gauge (a) and Water Particle Velocity Measure Device (b)

The motion and collision of the spheres were recorded with the 2 high-definition (1920x1080 pixels) video cameras. Sony RX-0 high-definition video camera with the 50 Hz sampling rate was placed on the top of the horizontal area, and the recordings taken from this video camera were used in the analysis stage. Sony FDR-X1000V video camera with the 25 Hz sampling rate was placed at the outlet of the horizontal area and recorded the experimental area for the extra video recordings in the case of need. The photographs for the cameras are shown in Figure 3.6.

(a) (b)

Figure 3.6: Top Camera (a) and Outlet Camera (b)

The video recording has to be clear enough to get the trajectories of the spheres accurately for the analysis stage. Therefore, one has to eliminate the external reflections created by the sunlight as well as the external lightning coming through the windows of the building. A metal cage was constructed at the top of the horizontal area for holding a black curtain as well as the camera placed on the top of the horizontal area. The black curtain eliminated nearly all of the external lights; therefore, 2 light sources were placed at the side of the experimental area to get homogeneous lightning for the physical experiments. Also, the impermeable horizontal area was covered with a checkerboard. The trajectory data of the spheres moving on the impermeable and porous horizontal area were calibrated with the checkerboard for the impermeable cases, and the distance between the holes on the punched metal sheet for the porous cases.

To sum up, there are 4 different experimental configurations that were used throughout this experimental study. The side views of these 4 different experimental configurations with the related case names and configuration parameters such as the slope inclination, the permeability of the bottom, water levels, and the exact locations of the slope, horizontal area and the instrumentations such as wave gauges (WG) and ADV are given in Figure 3.7. Also, the example photographs for the completed impermeable experimental setup are shown in Figure 3.8.

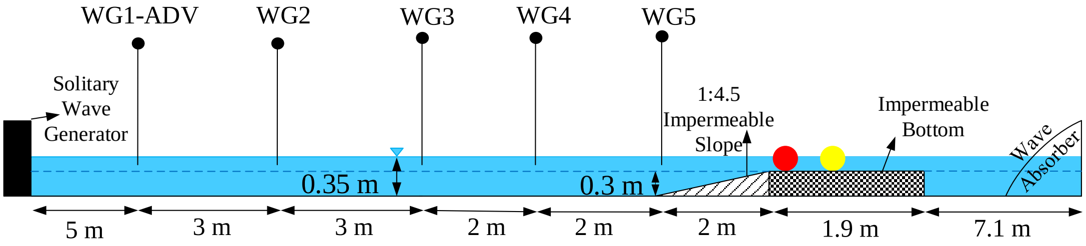

(a) Configuration 1: Case 1, Case 3, Case 5, Case 7

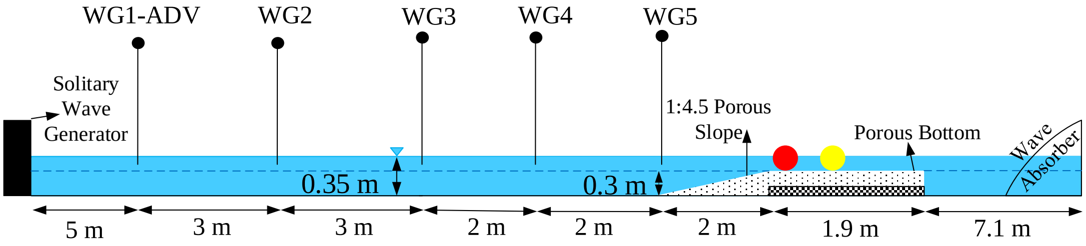

(b) Configuration 2: Case 2, Case 4, Case 6, Case 8

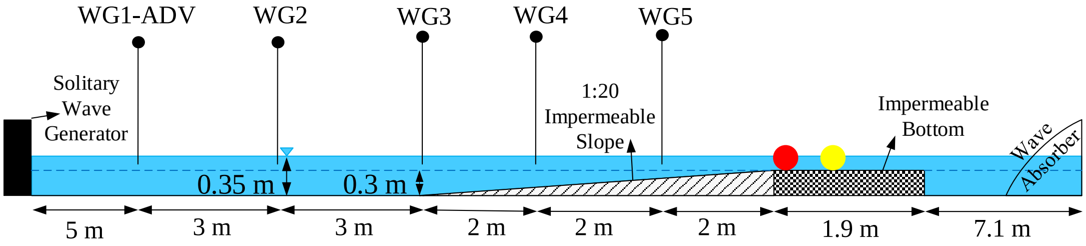

(c) Configuration 3: Case 9, Case 11, Case 13, Case 15

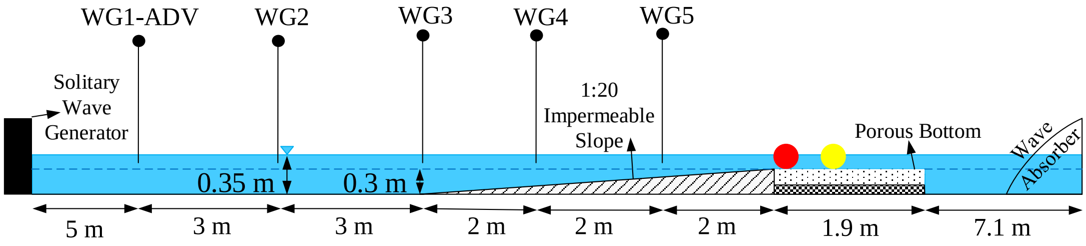

(d) Configuration 4: Case 10, Case 12, Case 14, Case 16

Figure 3.7: Side Views of the Experimental Setup for Different Configurations (Non-breaking Cases: a-b, Breaking Cases: c-d, Figure is not the scale!)

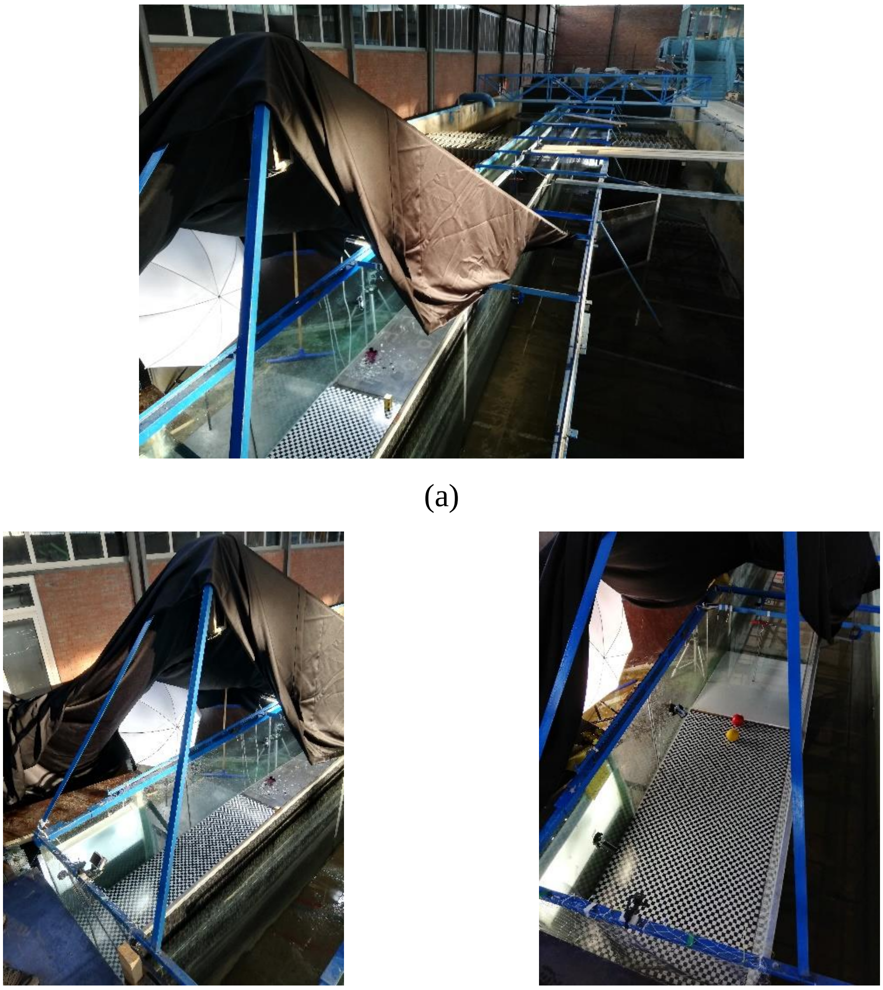

(a)

(b) (c)

Figure 3.8: Example Photographs for the Finished Experimental Setup: a and b) Impermeable Bottom (Configuration-3) c) Impermeable Bottom (Configuration-1)

3.4 Solitary Wave Generation

The solitary wave heights were investigated for the different water depths on each configuration. Malek-Mohammadi and Testik (2010) developed a solitary wave generation methodology, which is more useful and advantageous for both short and long laboratory setups than traditional solitary wave generation methodologies like developed by Goring (1979). Therefore, this method suggested by the Malek-Mohammadi and Testik (2010) for the piston-type wave generators was selected for the generation of the solitary waves as it gave the nearest desired solitary wave profile for the utilized wave channel. The equations taken from the referenced study are given as follows:

$$\frac{d\xi}{dt} = \sqrt{g * \frac{\eta_{wave}}{h_{water}} * \left(h_{water} + \frac{\eta_{wave}}{2}\right) + (\frac{\eta_{wave}}{h_{water} + \eta_{wave}})} \qquad \text{Eq. (3.3)}$$

$$\eta_{wave} = H * \sec h^2[k_{decay} * (c * t - \zeta)] \qquad \text{Eq. (3.4)}$$

Where $k_{decay} = \sqrt{(3 * H)/(4 * {h_{water}}^3)}$ and $c = \sqrt{g * (h_{water} + H)}$

The wave paddle trajectory can be calculated by Equation 3.3 where ζ is wave paddle trajectory, t is time, g is the acceleration of the gravity, h_{water} is the still water depth and η_{wave} is the wave profile for the solitary wave. Also, the solitary wave profile calculation with the Boussinesq method is given in Equation 3.4 where H is the solitary wave height, k_{decay} is the outskirt decay coefficient and c is the wave celerity. The solitary waves were generated with METU Wave Flume Wave Generation / Analysis Suite with the new methodology based on the Boussinesq's solution integrated with the Malek-Mohammadi and Testik (2010) approach.

The solitary wave analysis was performed from 15 cm solitary wave height to 8 cm solitary wave height for selecting the best solitary wave for dry and half-water conditions on each case. After the analysis, it was found that 15 cm solitary wave height is selected for the dry condition, whereas 13 cm solitary wave height selected for the half-water condition as these piston setups gave similar solitary wave height developing inside of the empty wave channel for the two different water levels. The piston positions for the generation of the solitary waves for the dry and half-water conditions are shown in Figure 3.9.

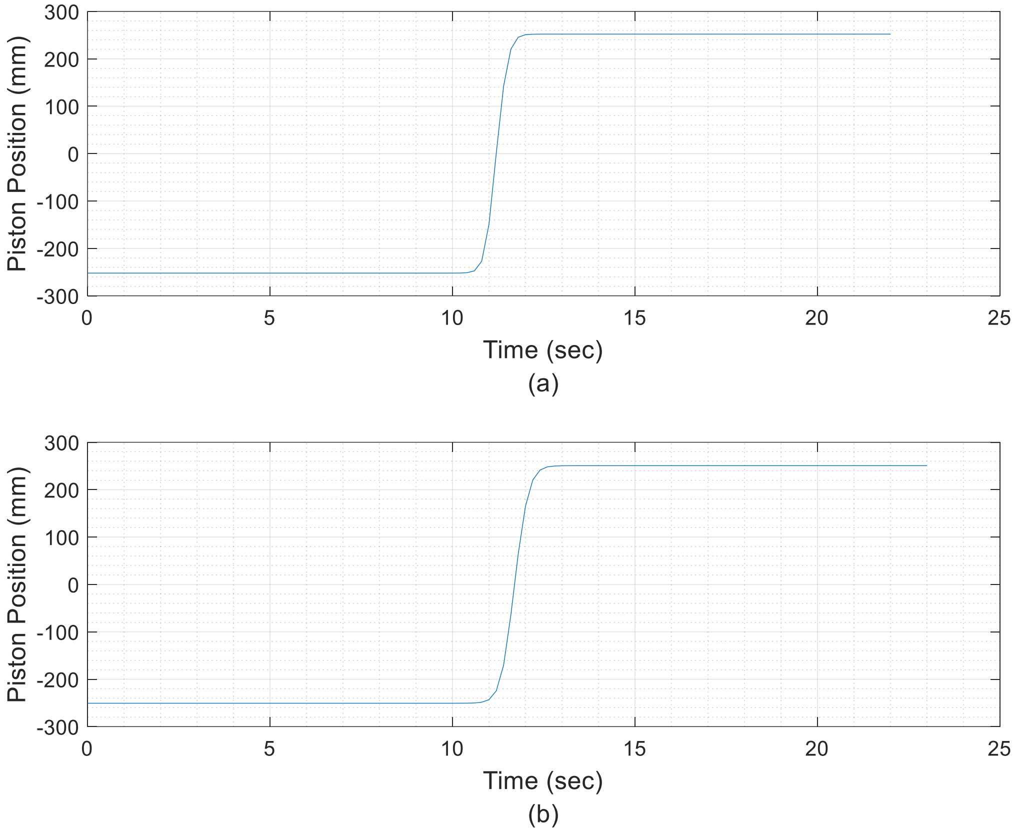

(a)

(b)

Figure 3.9: Piston Positions for Dry (a) and Half-Water (b) Conditions

3.5 Analysis of the Experiments

The video recordings of the top camera were used in the analysis of the experiments. As suggested in the Stolle et al. (2016), the experimental area was lighted intensively and homogeneously with the 2 light sources. Besides, the black curtain blocked the undesired external reflection and lights so that with the internal lighting, the quality of the video recordings of the experimental area was enriched intensively. The experimental videos were pre-processed with video editing software, and the unnecessary regions in the video recordings were trimmed from the video footage. Moreover, the unnecessary footages were trimmed from the timeline of the video recordings for reducing the analysis time. Later, these processed videos were cut into the frames and got ready for the path analysis of the spheres.

The paths of the spheres were tracked with the homemade image processing code by color detection algorithm that is similar to the one presented in Stolle et al. (2016). In the analysis stage, the lens originated distortions were checked with the help of the checkerboard, and it is seen that the lens originated distortions were neglectable. Also, the video frames were checked for the tilting due to the camera placement. If there is any, the video frames were rotated to the horizontal position with the help of the checkerboard and punched metal sheet for impermeable and porous cases, respectively. The mean calibration parameter for the pixel to mm transformation was checked on 3 different axes on the checkerboard and punched metal sheet for each repetition in each case. The example captions of the calibration stage for the impermeable and the porous bottom are shown in Figure 3.10.

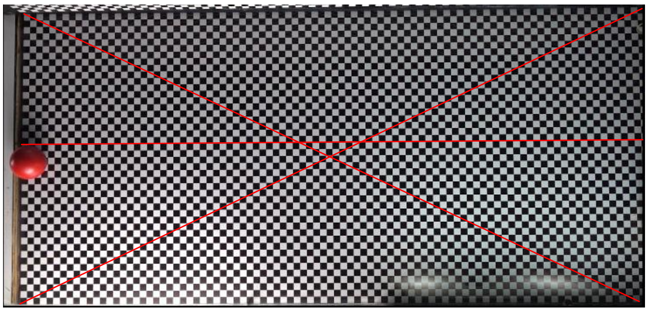

(a)

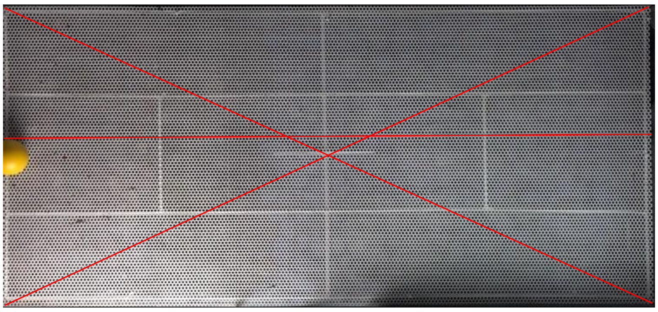

(b)

Figure 3.10: The Axes Used for the Calculation of the Mean Calibration Parameter for the Impermeable Bottom (a) and the Porous Bottom (b)

The color spectrum required to track the spheres were found with the trial and error approach. The spheres were isolated from the surroundings by adjusting the right color spectrum by trial and error, and the color spectrums for the yellow and red spheres were found for each case to better track the spheres by the color tracking algorithm. The example caption after the application of the exact color spectrum for the isolation of the single sphere from the surroundings is shown in Figure 3.11.

Figure 3.11: Example of Isolated Sphere by Adjusted Color Spectrum

The positions of the spheres in each frame were calculated by the centroid of the isolated sphere captions. It is seen from all the position data of the cases that the accuracy of the positions of the spheres was shifted up to 8 mm, mostly due to the poor tracking when the broken solitary wave was passing on the top of the spheres. This accuracy level is also close to the accuracy level mentioned in the Stolle et al. (2016). The sample captions of the tracked spheres on the impermeable and porous bottom are given in Figure 3.12, where the pink and black points show the centroid of the spheres which were found by the image processing algorithm.

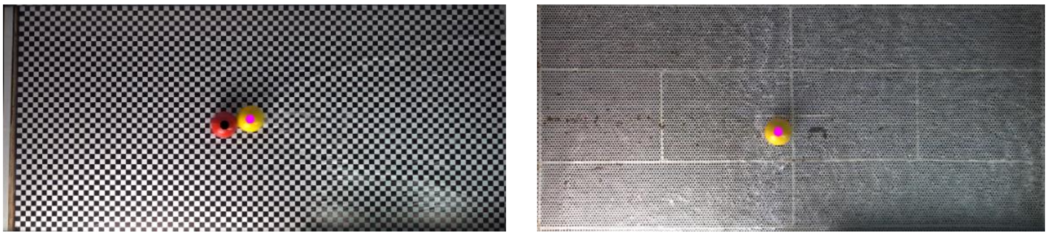

(a) (b)

Figure 3.12: Tracked Captions of the Spheres for the Impermeable Bottom (a) and the Porous Bottom (b)

The raw trajectory data of the 21 trials of each case were filtered with the spectrum analysis. The Fast Fourier Transform (FFT) technique was used for the elimination of the impurities from the trajectory data, such as the video camera distortions due to the sampling frequency. For doing this, the variance density spectrum of the 21 repetitions of each case was analyzed. From the results, it is seen that the frequencies above 2 Hz were considered as unrelated from the trajectory data of the spheres, and this portion of the data was removed by the low pass filter from all cases. The sample variance density spectrum for the selected 21 repetitions of one of the cases is shown in Figure 3.13.

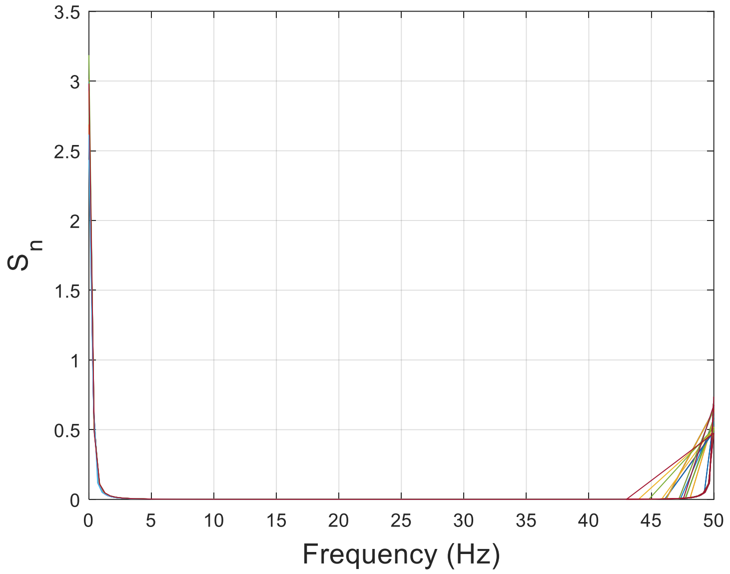

Figure 3.13: Sample Variance Density Spectrum

The filtered trajectory data for all of the 21 repetitions were used for the calculation of the velocities of the spheres in X-direction. Also, the trajectories and the computed velocities of the spheres were represented in dimensionless forms. The calculations of the dimensionless parameters are explained in the next section, which is Section 3.5.1, in detail.

3.5.1 Dimensionless Analysis

The calculations of the dimensionless parameters are shown below.

- Independent Variables: x (longitudinal dimension), y (transverse dimension), t (time), ρ (specific weight of water), g (gravitational force), h (water depth), ρ_s (density of the sphere), D (diameter of the sphere), H (solitary wave height)
- Dependent Variables: X (longitudinal displacement), Y (transverse displacement), $V_{s,x}$ (longitudinal velocity)

$$f_1(x, y, t, \rho, g, h, \rho_s, D, H, X, Y, V_x) = 0 \qquad \text{Eq. (3.5)}$$

ρ, g, D were selected as the basic parameters for the calculation of the dimensionless equations. Equation 3.6 shows the dimensional properties of the selected basic parameters. The calculations of the 3 different dependent equations are shown below. The Vaschy-Buckingham π theorem is used for the calculations of the dependent equations. The letters A, B and C show the power of the related independent dimensional parameter. The letter π represents the dimensionless dependent equation.

$$\rho = M^1 L^{-3} T^0 \quad g = M^0 L^1 T^{-2} \quad D = M^0 L^1 T^0$$
$$(M = Mass \quad L = Length \quad T = Time) \qquad \text{Eq. (3.6)}$$

$$\pi_X = \rho^{A_X} * g^{B_X} * D^{C_X} * X \qquad \text{Eq. (3.7-a)}$$

$$\pi_X = \frac{X}{D}\ (Dimensionless\ Longitudinal\ Displacement) \qquad \text{Eq. (3.7-b)}$$

$$\pi_Y = \rho^{A_Y} * g^{B_Y} * D^{C_Y} * Y \qquad \text{Eq. (3.8-a)}$$

$$\pi_Y = \frac{Y}{D}\ (Dimensionless\ Transverse\ Displacement) \qquad \text{Eq. (3.8-b)}$$

$$\pi_{v_{s,x}} = \rho^{A_{v_x}} * g^{B_{v_x}} * D^{C_{v_x}} * v_x \qquad \text{Eq. (3.9-a)}$$

$$\pi_{v_{s,x}} = \frac{v_{s,x}}{\sqrt{g * D}} (Dimensionless\ Longitudinal\ Velocity) \qquad \text{Eq. (3.9-b)}$$

$$f_2\left(\frac{x}{D}, \frac{y}{D}, t * \sqrt{\frac{g}{D}}, \frac{h}{D}, \frac{\rho_s}{\rho}, \frac{H}{D}, \frac{X}{D}, \frac{Y}{D}, \frac{V_{s,x}}{\sqrt{g * D}}\right) = 0 \qquad \text{Eq. (3.10)}$$

The dimensionless trajectories and dimensionless velocities of the cases were plotted with the mean and confidence band lines. The confidence band lines were added to the plots to present the uncertainty of the given results due to the diversity of the 21 repetitions of each case. Lütkepohl et al. (2013) examined the empirical literature and found out that the confidence band range has a lot of variety. Still, from the research, it is seen that most of the studies preferred to use the confidence band between the ranges 68% to 95%. Zhang and Yang (2017) examined different regression models and conducted a correlation curve analysis with these regression models. 95% confidence band was used as a limiting boundary on the results of the analysis. Also, Belov (2019) conducted a multiple linear normal regression analysis and used 95% confidence band for the mean of repeated observations. Therefore, the confidence band lines were set as 95%, which were located on the top and bottom of the mean line. Also, it is seen that nearly all of the experimental data for the 21 repetitions of each case were covered by this confidence band region.

CHAPTER 4

RESULTS

In this section, the water surface elevation and water particle velocity measurements are firstly given. After that, the trajectories and the velocities of the spheres are presented in terms of dimensionless parameters for each case showing the mean of the repetitions and the 95% confidence bands for the mean line.

4.1 Water Surface Elevation Measurements

The exact 5 locations of the installed wage gauges where the water surface elevations were measured along the wave channel are given in Figure 3.7 for each configuration. The measured water surface elevation data for the 5 different points were processed with the 5 Hz low pass filter using the FFT technique as exampled in Section 3.5, and the unintended noises were removed from the water surface elevation results. The water surface elevation measurements for the 30 and 35 cm water depths are presented in Figure 4.1 and Figure 4.2, respectively. The measurements showed that the configurations had no influence on the water surface elevation until the point WG4, as all of the readings were nearly identical until this point. Yet, except the water surface elevation readings for the non-breaking solitary wave cases where the readings at the WG5 point were nearly identical with the water surface elevation readings at other points, the water surface elevation readings for the breaking solitary wave cases were changing at the point WG5, as can be seen from the WG5 water surface elevation graphs for both 30 and 35 cm water depths. As the permeability of the slope and horizontal area change after the point WG4, as well as the solitary wave height changing due to the breaking process, the water surface elevations on the 2 different breaking solitary wave configurations were changed.

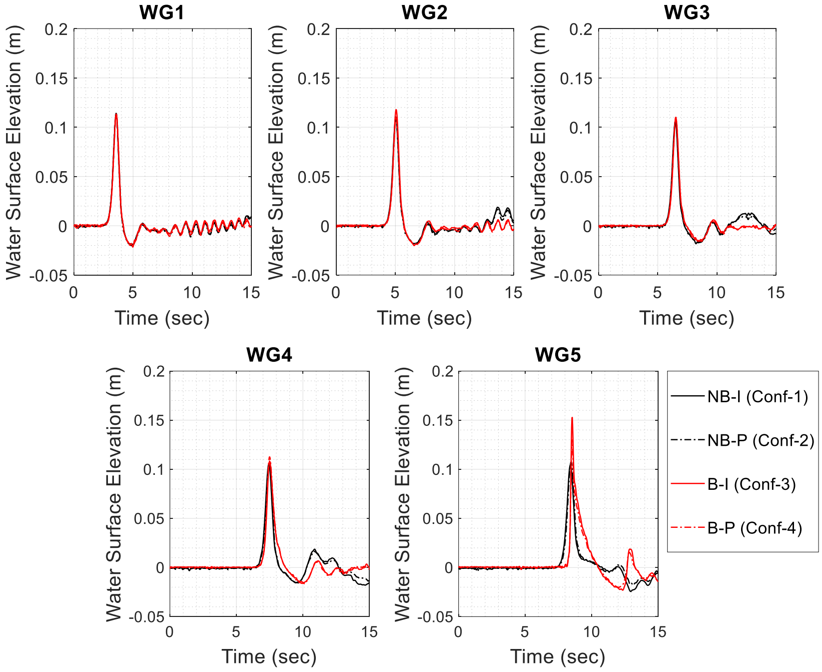

Figure 4.1: Water Surface Elevation Measurements at WG1-WG5 for Configurations 1-4 (Water Depth in front of the Wave Generator: 30 cm, NB: Non-Breaking Wave, B: Breaking Wave, I: Impermeable Base, P: Porous Base)

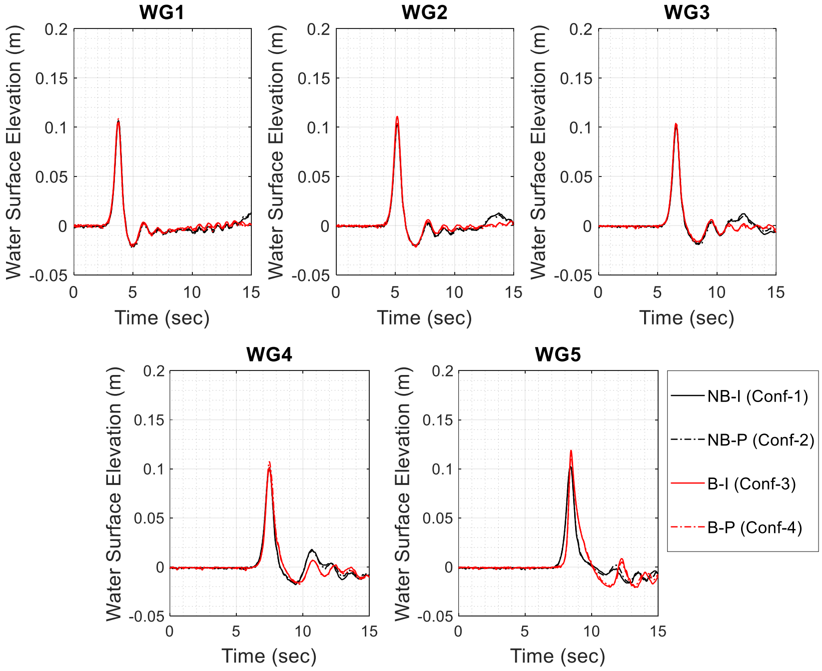

Figure 4.2: Water Surface Elevation Measurements at WG1-WG5 for Configurations 1-4 (Water Depth in front of the Wave Generator: 35 cm, NB: Non-Breaking Wave, B: Breaking Wave, I: Impermeable Base, P: Porous Base)

4.2 Water Particle Velocity Measurements

Water particle velocities created by the given solitary wave action were measured with an ADV. The ADV was installed 5 meters away from the solitary wave generator, where the WG1 wage gauge was also located at the same point shown in Figure 3.7. The water particle velocities at different water depths along the water column were measured for the 4 different configurations as the solitary waves passed. These results were processed with the 10 Hz low pass filter using the FFT technique as exampled in Section 3.5, and the unintended noises were removed from the water particle velocity results. After this filtering process, it is seen that there is no significant velocity change between the points across the velocity profile. Therefore, only the mean water particle velocities for each configuration are given in Figure 4.3 and Figure 4.4 for the 30 and 35 cm water depths, respectively. It is seen from these figures that the water particle velocities measured 5 meters away from the solitary wave generator were not affected significantly from the different configurations and water depths. Therefore, in addition to the water surface elevation results showing the solitary wave heights at WG1 point that were almost identical for the dry and half-water conditions, the water particle velocity results also indicate that the solitary waves were identical for the dry and half-water conditions. Also, these water particle velocity results can be used in the CFD applications as an additional data set.

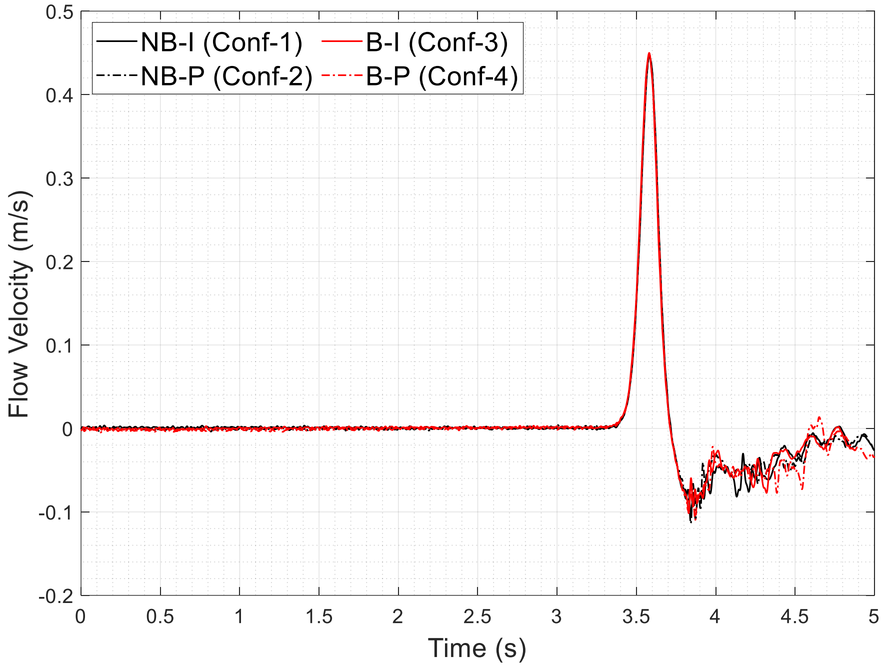

Figure 4.3: Mean Water Particle Velocity Measurements for Configurations 1-4 (Water Depth in front of the Wave Generator: 30 cm, NB: Non-Breaking Wave, B: Breaking Wave, I: Impermeable Base, P: Porous Base)

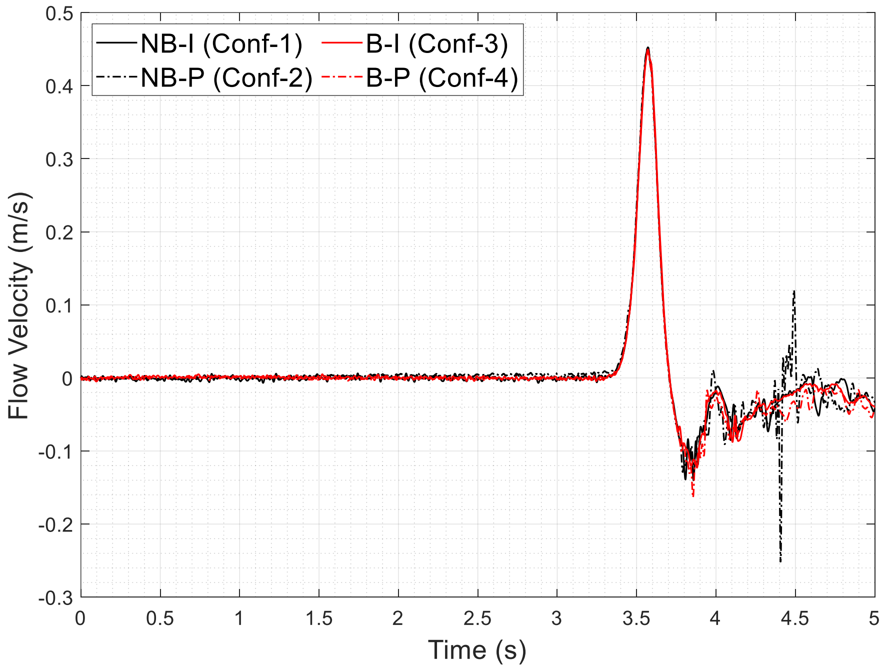

Figure 4.4: Mean Water Particle Velocity Measurements for Configurations 1-4 (Water Depth in front of the Wave Generator: 35 cm, NB: Non-Breaking Wave, B: Breaking Wave, I: Impermeable Base, P: Porous Base)

4.3 The Motion of the Spheres

The tracked trajectories and the computed velocities of the spheres from Case 1 up to Case 16 describing the motion of the spheres are presented in this section. The methodology described in Section 3.5 was used to track the trajectories of the spheres. Then, the trajectories of the spheres were used for the calculation of the velocities of the spheres along the X-axis. The trajectories and the computed velocities of the spheres were given in terms of dimensionless parameters. The dimensionless longitudinal displacement (X-Distance/D) and the dimensionless transverse displacement (Y-Distance/D) are given for the trajectory data. Also, the dimensionless velocity ($V_{s,x}/(g*D)^{0.5}$) is given for the computed longitudinal velocities of the spheres where D is the diameter of spheres, and g is the acceleration of gravity.

The overall motion of the spheres under the solitary wave attack is given in Figure 4.5, which presents the results of the two selected sample cases. In Figure 4.5, the mean line of the dimensionless velocities with respect to X-Distance/D for Case 1 (SP1-NB-S-DI: Single sphere, non-breaking solitary wave, dry and impermeable bottom) is represented as the black line and the mean line of the dimensionless velocities with respect to X-Distance/D for Case 3 (SP3-NB-S-HI: Single sphere, non-breaking solitary wave, half-water depth on impermeable bottom) is represented as the red line. All of the experimental setup configurations were the same for the cases shown in Figure 4.5, except the water levels, which was 30 cm for Case 1 and 35 cm for Case 3. The spheres in both cases were rolled without sliding and accelerated up to a certain point due to the solitary wave impact. After the terminal dimensionless velocity point, the sphere in Case 1 was continued its motion with almost constant dimensionless velocity, whereas the sphere in Case 3 was slowed down. It is seen from the results that the drag and inertia forces generated by the solitary waves are the main driving forces that generated the motion of the spheres in both cases. On the other hand, after the solitary wave attack, the energy of the spheres might be dissipated by rolling friction, air resistance and water resistance, which can lower the dimensionless velocity of the spheres along with their motion. According to Brilliantov and Pöschel (1999), the rolling friction becomes dominant if the speed of the sphere is lower than 10^{-2} m/s or the surface material of the bottom and/or the sphere are selected as a soft material, or these surface materials became softer. Witters and Duymelinck (1986) studied the air resistance and found out that the air resistance is smaller than the rolling friction for small-sized spheres, such as the spheres used in the present experiments. Therefore, from the studies mentioned above, the rolling friction and the air resistance forces are negligibly small for the present study. On the other hand, Figure 4.5 shows that the presence of the water body at different levels has a significant effect in damping the motion of the spheres. In Case 3 where the water level was initially at the half depth of the sphere, it can be seen that the friction drag generated by the water body slows down the motion of the sphere significantly. Furthermore, in addition to friction drag, the interaction between the solitary waves and spheres, as well as the solitary wave itself, create turbulence, which also affects the motion of the spheres.

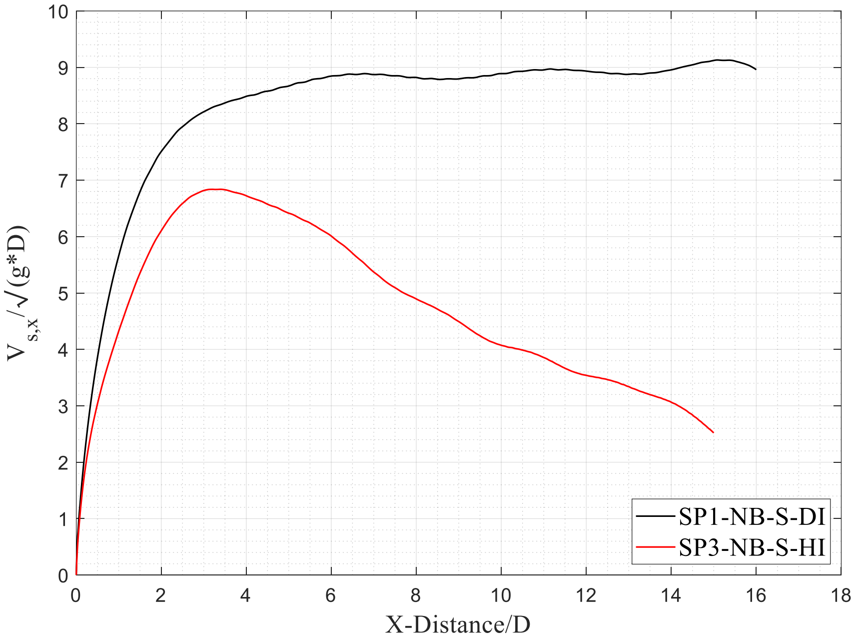

Figure 4.5: Effect of Dry and Half-Water Condition on the Motion of the Spheres (SP1-NB-S-DI: Single Sphere, Non-Breaking Solitary Wave, Dry and Impermeable Bottom - SP3-NB-S-HI: Single Sphere, Non-Breaking Solitary Wave, Half-Water Depth on Impermeable Bottom)

The results are presented in Figures 4.6 – 4.21, starting from Case 1 up to Case 16. These figures are given in terms of non-dimensional parameters stated in Section 3.5.1 and comprised of three different types of lines. In each figure, the grey lines represent each of 21 repetitions, whereas the black line is the mean line of the repetitions, and the red lines show the 95% confidence bands. Due to the limitations of the image processing analysis, the trajectories of the spheres could be tracked until a non-dimensional length of X/D=18, although the spheres were moving on the horizontal area that has the length of X/D=19. Therefore, the results are presented until X/D=18, as seen in Figures 4.6 - 4.21. The mean line and the confidence band lines are plotted until a selected X/D value due to two main reasons:

- The data lengths of the 21 repetitions of each case are not the same due to the different final positions of the spheres, which were a result of slight differences on the motion of the spheres on each repetition; therefore, the mean line and confidence band values cannot be computed as there is no equal data length for 21 repetitions.
- Experimental conditions created unrealistic disturbances on the motion of the spheres, and these unintended effects were created a significant bias on the results after the selected X/D values. The reasons behind the unrealistic disturbances in the experimental data are listed as follows:
    - Although most of the wave reflections were absorbed by the wave absorbers, which were placed at the end of the wave channel, the motion of the spheres was mostly disturbed by the wave reflections, which were reflected from the wave absorbers. (e.g., Case 3 presented in Figure 4.8 and Case 5 presented in Figure 4.10).
    - The irregularities on the surface of the porous horizontal area constructed with the rubble stones had an important effect on the trajectories of the spheres (e.g., Case 10 presented in Figure 4.15).

  - The net installed at the end of the horizontal area due to the reasons mentioned in Section 3.2 enables spheres to bounce back from the end of the horizontal area. Therefore, trajectories of the inlet and outlet spheres at the outlet region of the horizontal area were affected mostly due to the collisions of the spheres in double sphere cases as the outlet sphere was bounced back and hit the inlet sphere. (e.g., Case 6 presented in Figure 4.11).

The effects mentioned above are considered as unrealistic as they are not related to the motion of the spheres under a solitary wave attack. For example, the spheres would not bounce back if there is no net installed at the end of the horizontal area. Therefore, one cannot observe an unrealistic collision due to the bounced back outlet sphere, and this cannot create an unrealistic disturbance on the results. However, as the reasons are stated in Section 3.2, it is not possible to remove the net installed at the end of the horizontal area. Therefore, these disturbances are not considered in describing the motion of the spheres under a solitary wave attack. On the other hand, for the information of the reader, the whole of the experimental data represented by the grey lines are given until X/D=18 for all of the cases; however, the motions of the spheres are investigated until the selected X/D values in the present study. Moreover, it is recommended to use the experimental data up to the selected X/D values for numerical simulation purposes.

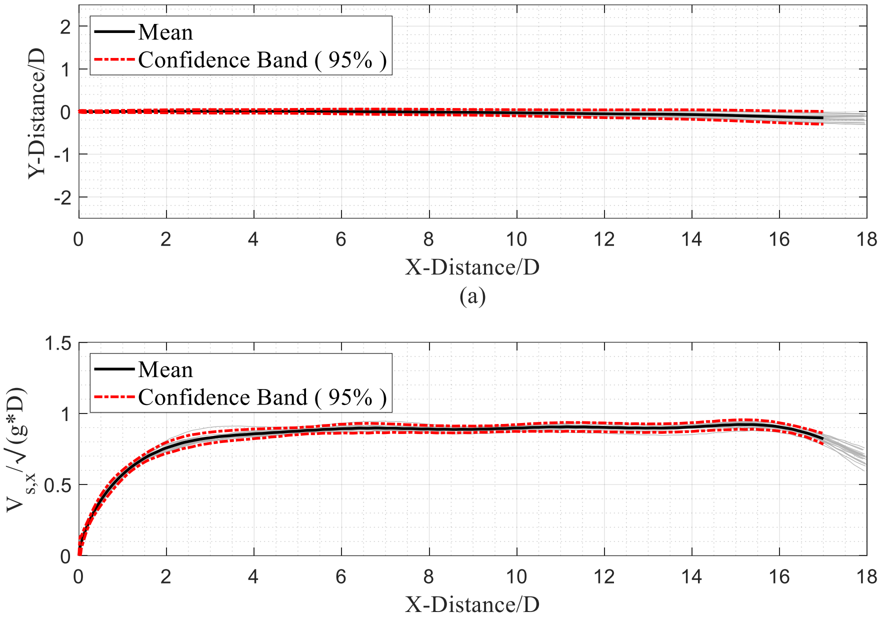

(a)

(b)

Figure 4.6: Results of Case 1 (SP1-NB-S-DI: Single Sphere under Non-Breaking Wave Attack on the Impermeable Slope and Impermeable Horizontal Area for Dry Condition) (a) Dimensionless Trajectory and (b) Dimensionless Velocity

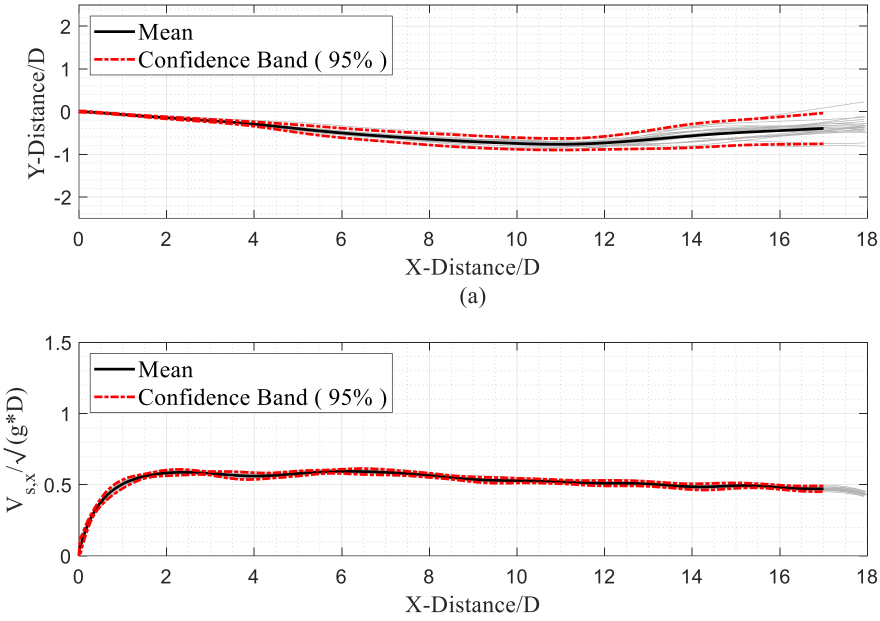

(a)

(b)

Figure 4.7: Results of Case 2 (SP2-NB-S-DP: Single Sphere under Non-Breaking Wave Attack on the Porous Slope and Porous Horizontal Area for Dry Condition) (a) Dimensionless Trajectory and (b) Dimensionless Velocity

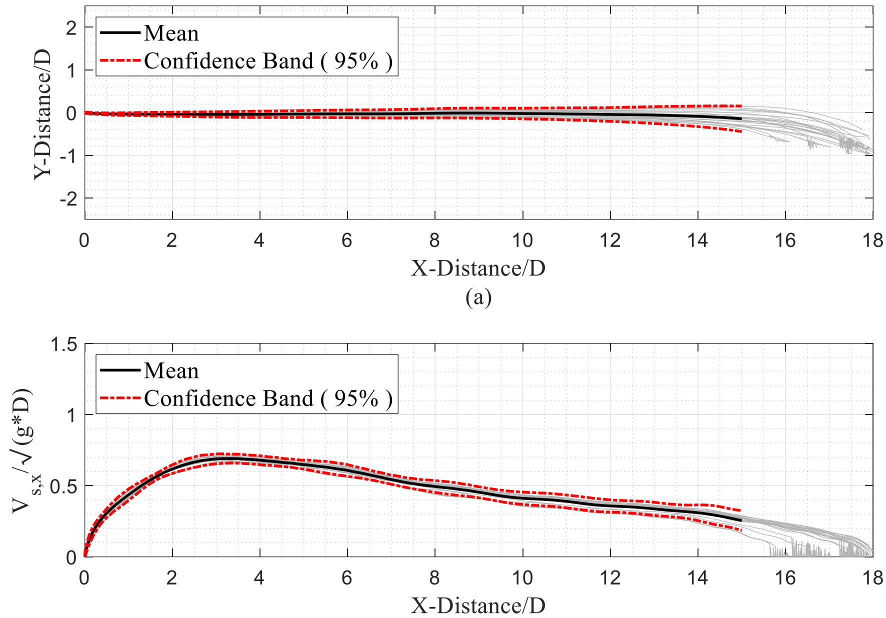

(a)

(b)

Figure 4.8: Results of Case 3 (SP3-NB-S-HI: Single Sphere under Non-Breaking Wave Attack on the Impermeable Slope and Impermeable Horizontal Area for Half-Water Condition) (a) Dimensionless Trajectory and (b) Dimensionless Velocity

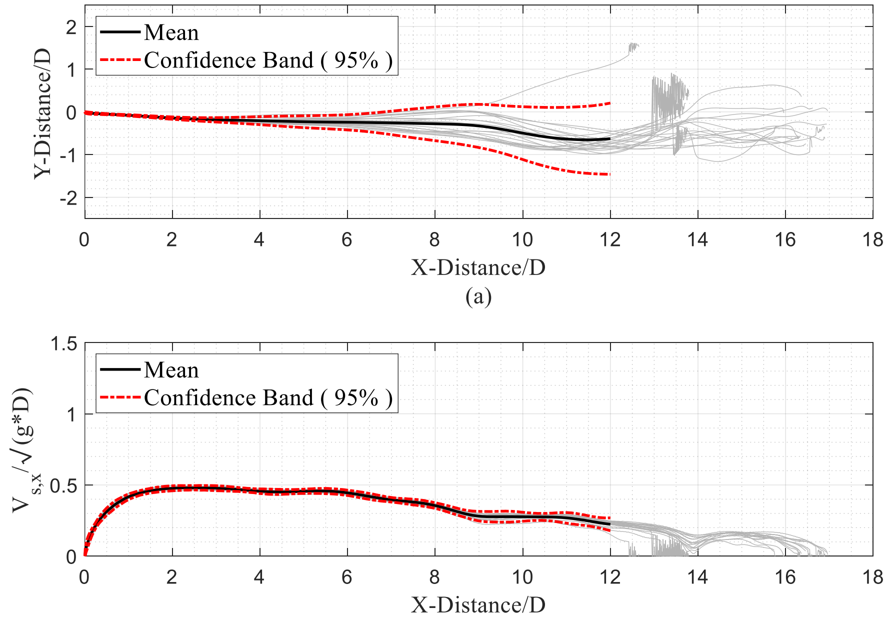

(a)

(b)

Figure 4.9: Results of Case 4 (SP4-NB-S-HP: Single Sphere under Non-Breaking Wave Attack on the Porous Slope and Porous Horizontal Area for Half-Water Condition) (a) Dimensionless Trajectory and (b) Dimensionless Velocity

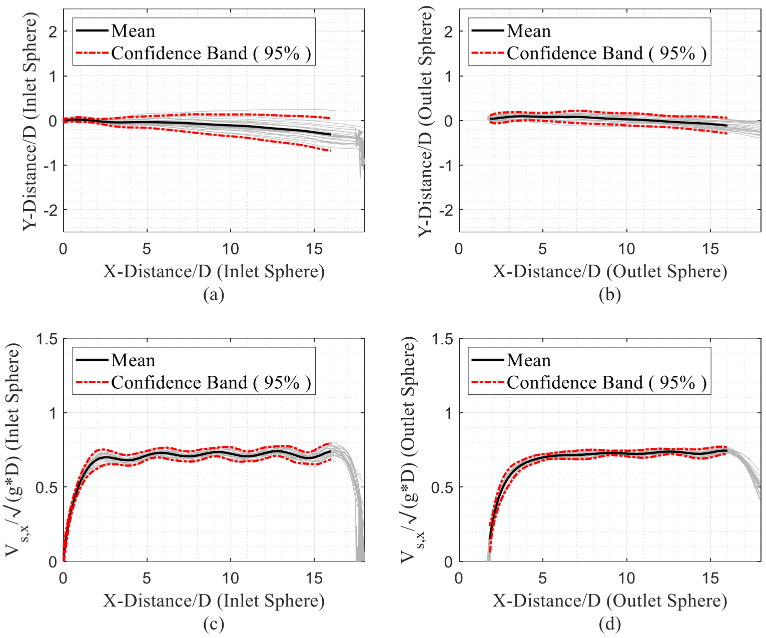

(a) (b) (c) (d)

Figure 4.10: Results of Case 5 (SP5-NB-T-DI: Two Spheres under Non-Breaking Wave Attack on the Impermeable Slope and Impermeable Horizontal Area for Dry Condition) (a-b) Dimensionless Trajectory and (c-d) Dimensionless Velocity for Inlet and Outlet Spheres

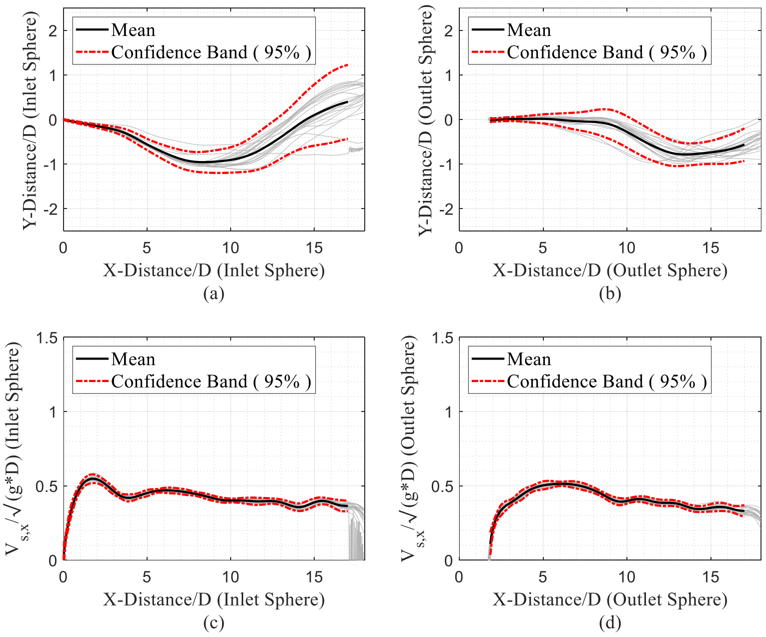

(a) (b) (c) (d)

Figure 4.11: Results of Case 6 (SP6-NB-T-DP: Two Spheres under Non-Breaking Wave Attack on the Porous Slope and Porous Horizontal Area for Dry Condition) (a-b) Dimensionless Trajectory and (c-d) Dimensionless Velocity for Inlet and Outlet Spheres

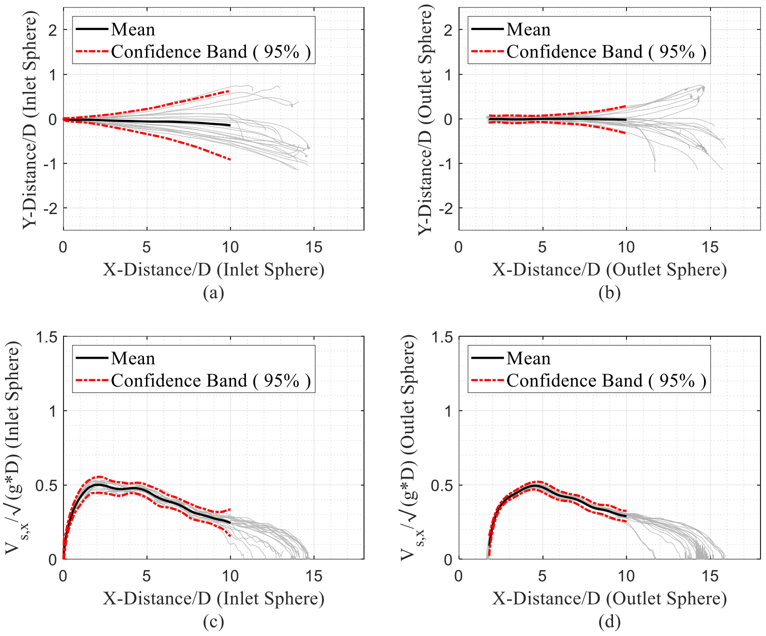

Figure 4.12: Results of Case 7 (SP7-NB-T-HI: Two Spheres under Non-Breaking Wave Attack on the Impermeable Slope and Impermeable Horizontal Area for Half-Water Condition) (a-b) Dimensionless Trajectory and (c-d) Dimensionless Velocity for Inlet and Outlet Spheres

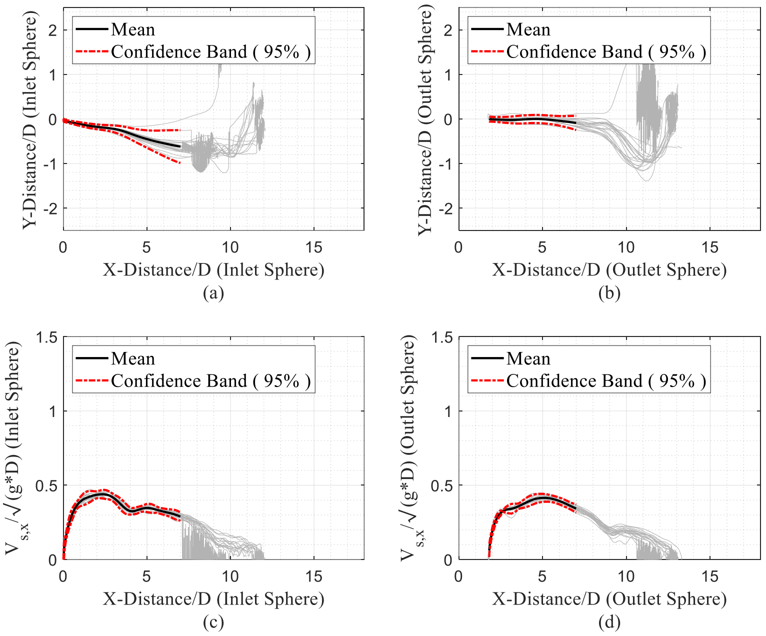

Figure 4.13: Results of Case 8 (SP8-NB-T-HP: Two Spheres under Non-Breaking Wave Attack on the Porous Slope and Porous Horizontal Area for Half-Water Condition) (a-b) Dimensionless Trajectory and (c-d) Dimensionless Velocity for Inlet and Outlet Spheres

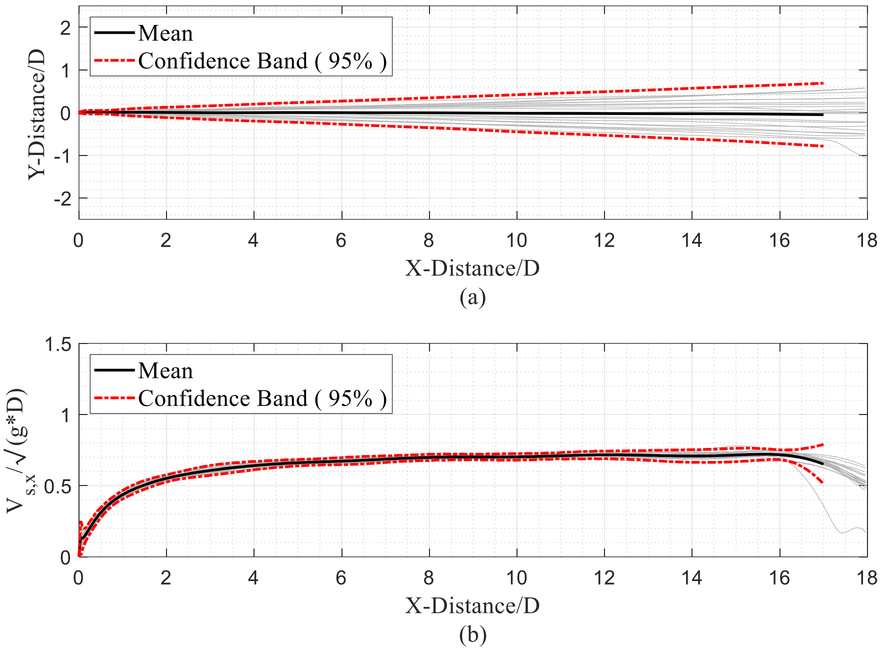

Figure 4.14: Results of Case 9 (SP9-B-S-DI: Single Sphere under Breaking Wave Attack on the Impermeable Slope and Impermeable Horizontal Area for Dry Condition) (a) Dimensionless Trajectory and (b) Dimensionless Velocity

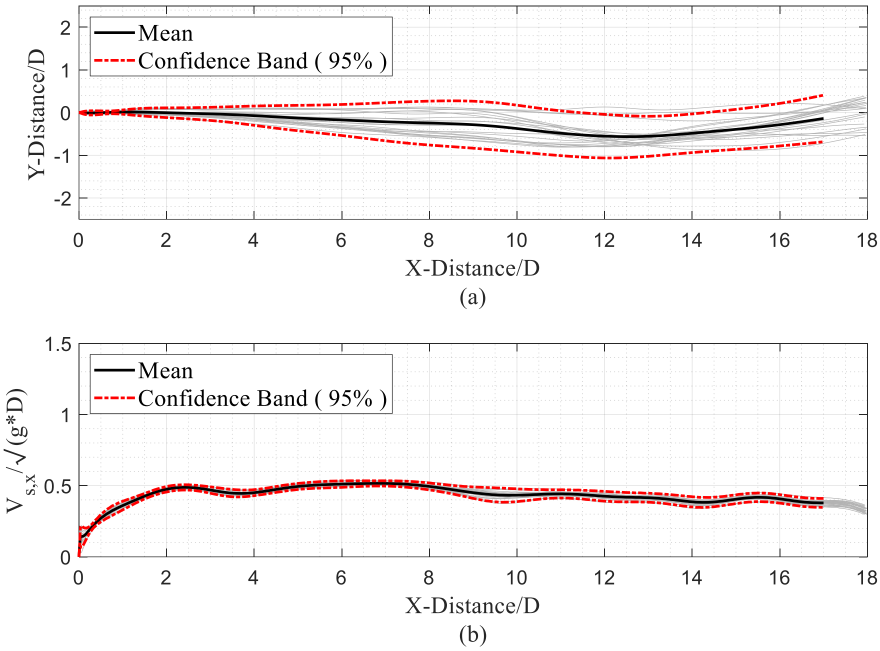

Figure 4.15: Results of Case 10 (SP10-B-S-DP: Single Sphere under Breaking Wave Attack on the Impermeable Slope and Porous Horizontal Area for Dry Condition) (a) Dimensionless Trajectory and (b) Dimensionless Velocity

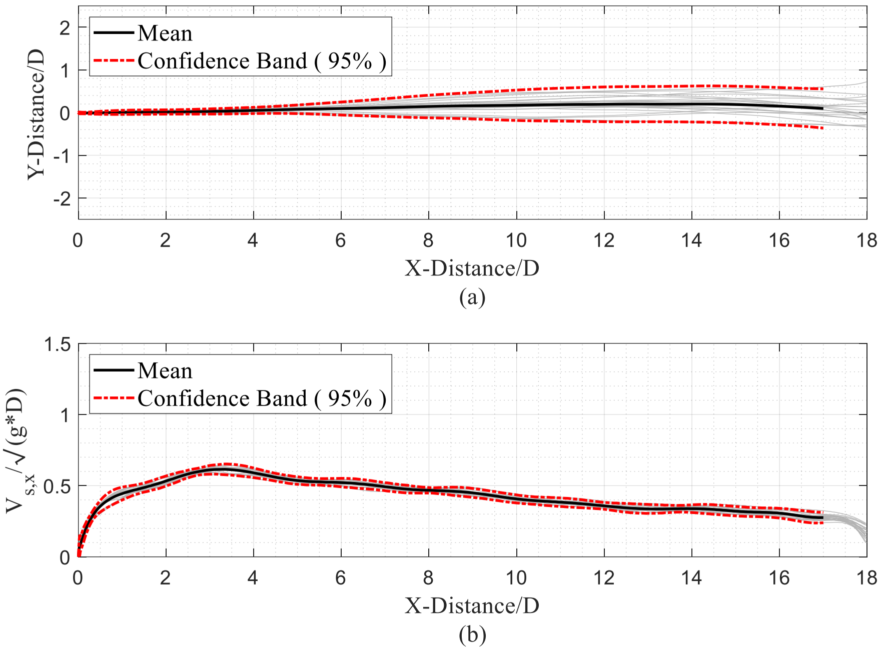

(a)

(b)

Figure 4.16: Results of Case 11 (SP11-B-S-HI: Single Sphere under Breaking Wave Attack on the Impermeable Slope and Impermeable Horizontal Area for Half-Water Condition) (a) Dimensionless Trajectory and (b) Dimensionless Velocity

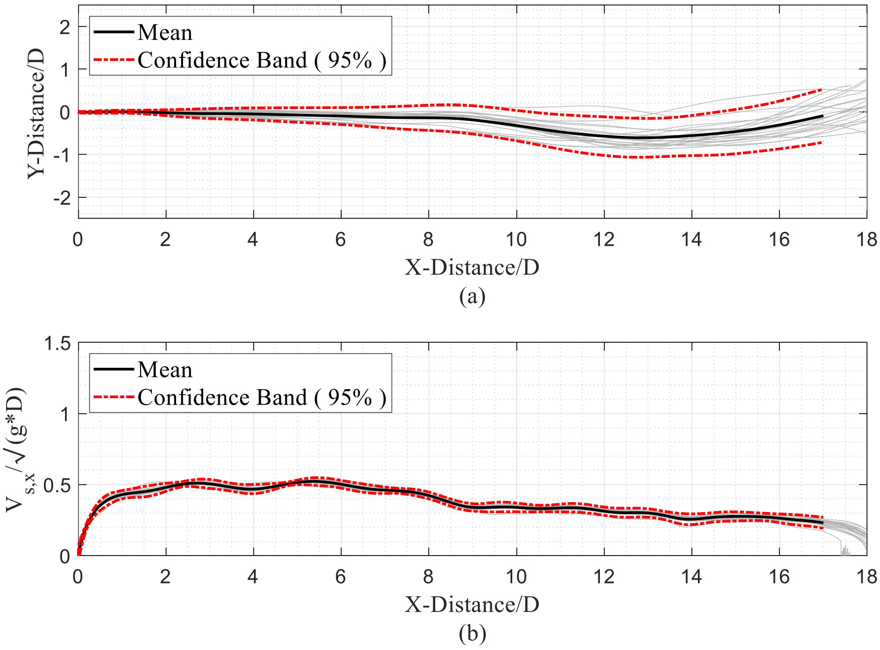

(a)

(b)

Figure 4.17: Results of Case 12 (SP12-B-S-HP: Single Sphere under Breaking Wave Attack on the Impermeable Slope and Porous Horizontal Area for Half-Water Condition) (a) Dimensionless Trajectory and (b) Dimensionless Velocity

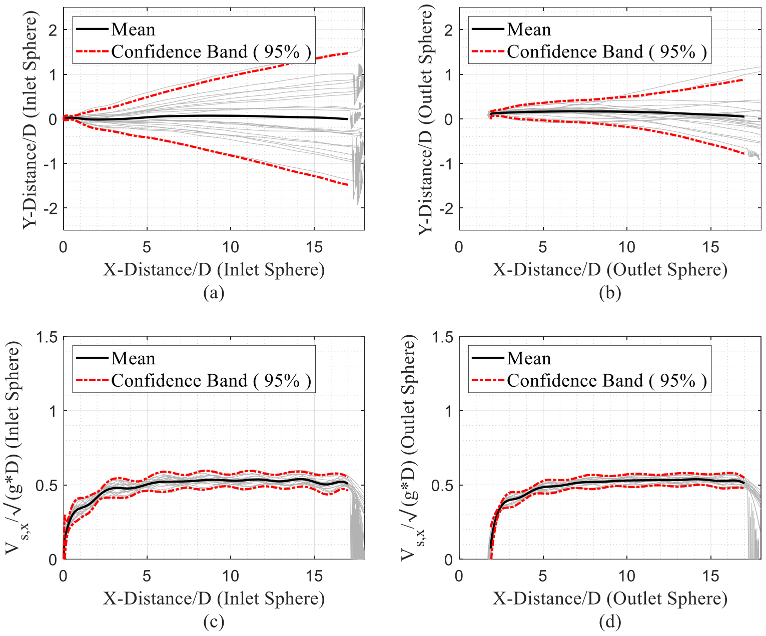

Figure 4.18: Results of Case 13 (SP13-B-T-DI: Two Spheres under Breaking Wave Attack on the Impermeable Slope and Impermeable Horizontal Area for Dry Condition) (a-b) Dimensionless Trajectory and (c-d) Dimensionless Velocity for Inlet and Outlet Spheres

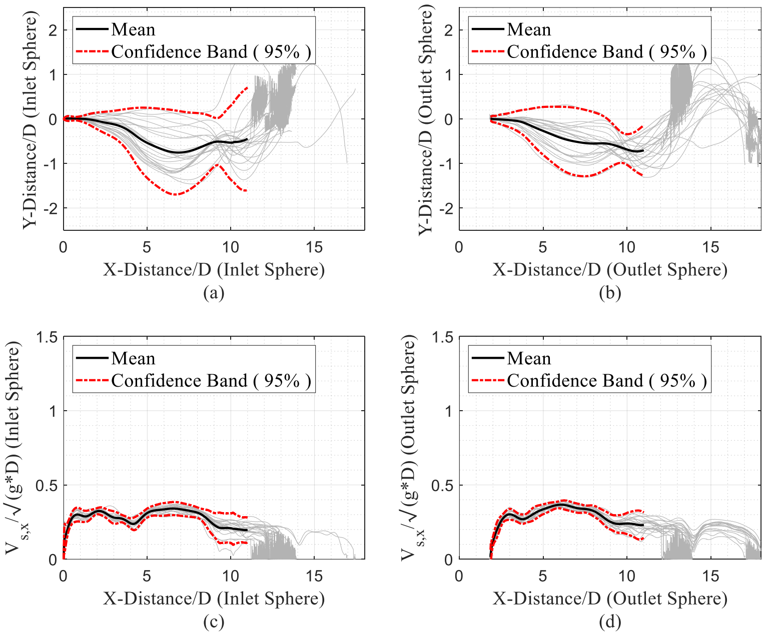

Figure 4.19: Results of Case 14 (SP14-B-T-DP: Two Spheres under Breaking Wave Attack on the Impermeable Slope and Porous Horizontal Area for Dry Condition) (a-b) Dimensionless Trajectory and (c-d) Dimensionless Velocity for Inlet and Outlet Spheres

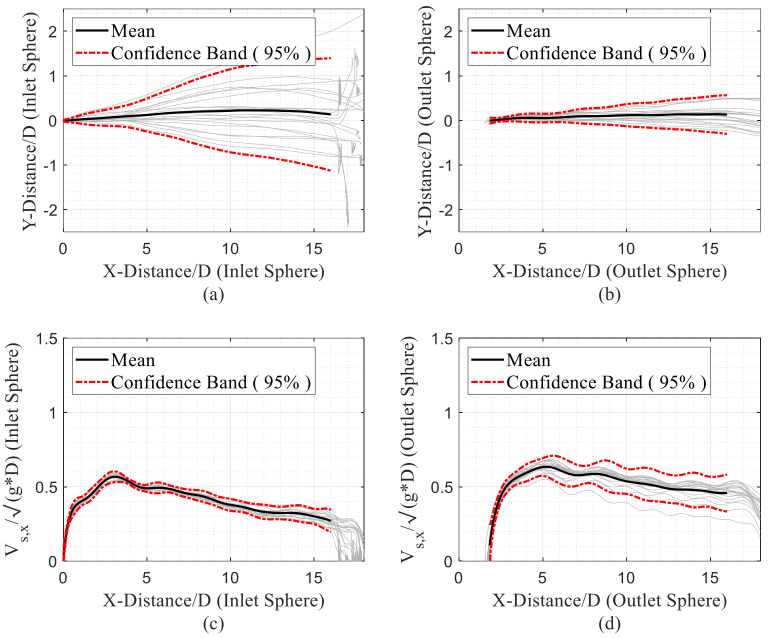

Figure 4.20: Results of Case 15 (SP15-B-T-HI: Two Spheres under Breaking Wave Attack on the Impermeable Slope and Impermeable Horizontal Area for Half-Water Condition) (a-b) Dimensionless Trajectory and (c-d) Dimensionless Velocity for Inlet and Outlet Spheres

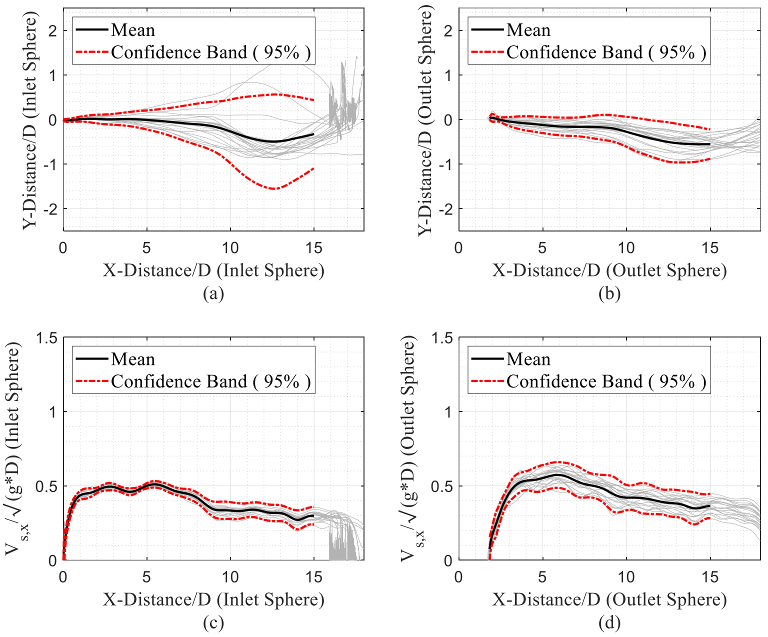

Figure 4.21: Results of Case 16 (SP16-B-T-HP: Two Spheres under Breaking Wave Attack on the Impermeable Slope and Porous Horizontal Area for Half-Water Condition) (a-b) Dimensionless Trajectory and (c-d) Dimensionless Velocity for Inlet and Outlet Spheres

CHAPTER 5

DISCUSSION OF THE RESULTS

The results presented in Figures 4.6 – 4.21 are interpreted using three parameters:

i) Deviation Along Y-axis,

ii) Terminal Dimensionless Velocity and

iii) Rate of Damping

The deviation along the Y-axis is given to better express how the experimental conditions affect the trajectories of the spheres. For doing this, the uppermost and the lowermost locations of the mean trajectory data of the spheres with respect to the Y-axis are represented as the deviation along the Y-axis.

The terminal dimensionless velocity is given to investigate the initial behavior of the spheres due to the experimental conditions and presented with their standard deviation. The terminal dimensionless velocity is defined as the first point, where the gradient between successive points on the mean dimensionless velocity data becomes less than 1%.

The rate of damping is taken into consideration to distinguish how the experimental conditions affect the motion of the spheres after the location where the terminal dimensionless velocity is computed. The slope of the line fitted to mean dimensionless velocity data between the terminal and final dimensionless velocities of the spheres is determined as the rate of damping value.

The deviation along the Y-axis, the terminal dimensionless velocity and the rate of damping parameters are calculated for each case and presented in Table 5.1 and Table 5.2 for the single sphere cases and double sphere cases, respectively. In addition to the given parameters, the selected X/D values, which are the unique final X/D values of the mean and confidence band lines for each case, are given in Table

5.1 and 5.2. In Table 5.2, it is also indicated that whether the spheres have collided or not due to the possibility of the collision in double sphere cases. The percent relative changes between the cases affected from the 3 main conditions are given in Table 5.3, Table 5.4 and Table 5.5 for the impermeable/porous bottom, the dry/half-water condition and non-breaking/breaking solitary wave type, respectively. Based on these results presented in Table 5.1, Table 5.2, Table 5.3, Table 5.4 and Table 5.5, the discussions are carried out in four subsections. In the first three subsections, the results are discussed in categories, namely impermeable/porous bottom, dry/half-water condition, and non-breaking/breaking solitary waves. In the final subsection, the collision behavior of the double sphere cases is assessed.

Table 5.1: Parameters Calculated for Single Sphere Cases

		Deviation Along Y-axis (Y/D)	**Terminal Dimensionless Velocity on X-axis ± Standard Deviation**	**Rate of Damping**	**Final X/D Values of Mean and Confidence Band Lines**
Non-Breaking Cases (Case No)	**SP1-NB-S-DI (Case 1)**	[0.006 -0.146]	0.897 ± 0.032	0.000	17
	SP2-NB-S-DP (Case 2)	[0 -0.766]	0.587 ± 0.020	-0.009	17
	SP3-NB-S-HI (Case 3)	[0 -0.146]	0.690 ± 0.033	-0.038	15
	SP4-NB-S-HP (Case 4)	[0 -0.654]	0.480 ± 0.016	-0.030	12
Breaking Cases (Case No)	**SP9-B-S-DI (Case 9)**	[0.010 -0.050]	0.697 ± 0.021	0.000	17
	SP10-B-S-DP (Case 10)	[0.012 -0.564]	0.488 ± 0.019	-0.008	17
	SP11-B-S-HI (Case 11)	[0.200 -0.011]	0.615 ± 0.037	-0.023	17
	SP12-B-S-HP (Case 12)	[0.002 -0.610]	0.510 ± 0.027	-0.022	17

Table 5.2: Parameters Calculated for Double Sphere Cases

			Deviation Along Y-axis (Y/D)	Terminal Dimensionless Velocity on X-axis ± Standard Deviation	Rate of Damping	Final X/D Values of Mean and Confidence Band Lines	Collision of Spheres
Non-Breaking Cases (Case No)	**SP5-NB-T-DI (Case 5)**	**Inlet Sphere**	[0.020 -0.314]	0.700 ± 0.051	0.002	16	✓
		Outlet Sphere	[0.093 -0.116]	0.712 ± 0.022	0.002		
	SP6-NB-T-DP (Case 6)	**Inlet Sphere**	[0.397 -0.956]	0.548 ± 0.029	-0.008	17	✓
		Outlet Sphere	[0.014 -0.784]	0.513 ± 0.015	-0.016		
	SP7-NB-T-HI (Case 7)	**Inlet Sphere**	[0 -0.147]	0.501 ± 0.053	-0.036	10	✓
		Outlet Sphere	[0.001 -0.019]	0.494 ± 0.026	-0.039		
	SP8-NB-T-HP (Case 8)	**Inlet Sphere**	[0 -0.619]	0.439 ± 0.028	-0.027	7	✓
		Outlet Sphere	[0 -0.09]	0.415 ± 0.028	-0.038		
Breaking Cases (Case No)	**SP13-B-T-DI (Case 13)**	**Inlet Sphere**	[0.071 -0.015]	0.479 ± 0.066	0.002	17	✓
		Outlet Sphere	[0.170 0]	0.490 ± 0.045	0.002		
	SP14-B-T-DP (Case 14)	**Inlet Sphere**	[0.008 -0.756]	0.296 ± 0.043	-0.008	11	✓
		Outlet Sphere	[0.005 -0.730]	0.302 ± 0.037	-0.011		
	SP15-B-T-HI (Case 15)	**Inlet Sphere**	[0.226 -0.006]	0.567 ± 0.036	-0.022	16	✗
		Outlet Sphere	[0.139 -0.003]	0.635 ± 0.063	-0.017		
	SP16-B-T-HP (Case 16)	**Inlet Sphere**	[0.016 -0.496]	0.495 ± 0.024	-0.021	15	✗
		Outlet Sphere	[0.038 -0.556]	0.573 ± 0.086	-0.025		

Table 5.3: Percent Relative Change Between the Cases in Impermeable and Porous Bottom Conditions

<table>
<tr><th colspan="6">SINGLE SPHERE CASES</th></tr>
<tr><th>Water Level</th><th>Solitary Wave Type</th><th colspan="2">Compared Cases (Impermeable vs. Porous)</th><th>Percent Relative Change in Terminal Dimensionless Velocity (%)</th><th>Percent Relative Change in Rate of Damping (%)</th></tr>
<tr><td>Dry</td><td>Non-Breaking</td><td colspan="2">SP1 vs. SP2</td><td>52,81</td><td>-100,00</td></tr>
<tr><td>Dry</td><td>Breaking</td><td colspan="2">SP9 vs. SP10</td><td>42,83</td><td>-100,00</td></tr>
<tr><td>Half-Water</td><td>Non-Breaking</td><td colspan="2">SP3 vs. SP4</td><td>43,75</td><td>26,67</td></tr>
<tr><td>Half-Water</td><td>Breaking</td><td colspan="2">SP11 vs. SP12</td><td>20,59</td><td>4,55</td></tr>
<tr><th colspan="6">DOUBLE SPHERE CASES</th></tr>
<tr><th>Water Level</th><th>Solitary Wave Type</th><th colspan="2">Compared Cases (Impermeable vs. Porous)</th><th>Percent Relative Change in Terminal Dimensionless Velocity (%)</th><th>Percent Relative Change in Rate of Damping (%)</th></tr>
<tr><td rowspan="2">Dry</td><td rowspan="2">Non-Breaking</td><td rowspan="2">SP5 vs. SP6</td><td>Inlet Sphere</td><td>27,74</td><td>-125,00</td></tr>
<tr><td>Outlet Sphere</td><td>38,79</td><td>-112,50</td></tr>
<tr><td rowspan="2">Dry</td><td rowspan="2">Breaking</td><td rowspan="2">SP13 vs. SP14</td><td>Inlet Sphere</td><td>61,82</td><td>-125,00</td></tr>
<tr><td>Outlet Sphere</td><td>62,25</td><td>-118,18</td></tr>
<tr><td rowspan="2">Half-Water</td><td rowspan="2">Non-Breaking</td><td rowspan="2">SP7 vs. SP8</td><td>Inlet Sphere</td><td>14,12</td><td>33,33</td></tr>
<tr><td>Outlet Sphere</td><td>19,04</td><td>2,63</td></tr>
<tr><td rowspan="2">Half-Water</td><td rowspan="2">Breaking</td><td rowspan="2">SP15 vs. SP16</td><td>Inlet Sphere</td><td>14,55</td><td>4,76</td></tr>
<tr><td>Outlet Sphere</td><td>10,82</td><td>-32,00</td></tr>
</table>

Table 5.4: Percent Relative Change Between the Cases in Dry and Half-Water Conditions

<table>
<tr><th colspan="6">SINGLE SPHERE CASES</th></tr>
<tr><th>Bottom Porosity</th><th>Solitary Wave Type</th><th colspan="2">Compared Cases (Dry vs. Half-Water)</th><th>Percent Relative Change in Terminal Dimensionless Velocity (%)</th><th>Percent Relative Change in Rate of Damping (%)</th></tr>
<tr><td>Impermeable</td><td>Non-Breaking</td><td colspan="2">SP1 vs. SP3</td><td>30,00</td><td>-100,00</td></tr>
<tr><td>Impermeable</td><td>Breaking</td><td colspan="2">SP9 vs. SP11</td><td>13,33</td><td>-100,00</td></tr>
<tr><td>Porous</td><td>Non-Breaking</td><td colspan="2">SP2 vs. SP4</td><td>22,29</td><td>-70,00</td></tr>
<tr><td>Porous</td><td>Breaking</td><td colspan="2">SP10 vs. SP12</td><td>-4,31</td><td>-63,64</td></tr>
<tr><th colspan="6">DOUBLE SPHERE CASES</th></tr>
<tr><th>Bottom Porosity</th><th>Solitary Wave Type</th><th colspan="2">Compared Cases (Dry vs. Half-Water)</th><th>Percent Relative Change in Terminal Dimensionless Velocity (%)</th><th>Percent Relative Change in Rate of Damping (%)</th></tr>
<tr><td rowspan="2">Impermeable</td><td rowspan="2">Non-Breaking</td><td rowspan="2">SP5 vs. SP7</td><td>Inlet Sphere</td><td>39,72</td><td>-105,56</td></tr>
<tr><td>Outlet Sphere</td><td>44,13</td><td>-105,13</td></tr>
<tr><td rowspan="2">Impermeable</td><td rowspan="2">Breaking</td><td rowspan="2">SP13 vs. SP15</td><td>Inlet Sphere</td><td>-15,52</td><td>-109,09</td></tr>
<tr><td>Outlet Sphere</td><td>-22,83</td><td>-111,76</td></tr>
<tr><td rowspan="2">Porous</td><td rowspan="2">Non-Breaking</td><td rowspan="2">SP6 vs. SP8</td><td>Inlet Sphere</td><td>24,83</td><td>-70,37</td></tr>
<tr><td>Outlet Sphere</td><td>23,61</td><td>-57,89</td></tr>
<tr><td rowspan="2">Porous</td><td rowspan="2">Breaking</td><td rowspan="2">SP14 vs. SP16</td><td>Inlet Sphere</td><td>-40,20</td><td>-61,90</td></tr>
<tr><td>Outlet Sphere</td><td>-47,29</td><td>-56,00</td></tr>
</table>

Table 5.5: Percent Relative Change Between the Cases in Non-Breaking and Breaking Solitary Wave Conditions

SINGLE SPHERE CASES

Bottom Porosity	Water Level	Compared Cases (Non-Breaking vs. Breaking)	Percent Relative Change in Terminal Dimensionless Velocity (%)	Percent Relative Change in Rate of Damping (%)
Impermeable	Dry	SP1 vs. SP9	28,69	NA
Impermeable	Half-Water	SP3 vs. SP11	12,20	65,22
Porous	Dry	SP2 vs. SP10	20,29	12,50
Porous	Half-Water	SP4 vs. SP12	-5,88	36,36

DOUBLE SPHERE CASES

Bottom Porosity	Water Level	Compared Cases (Non-Breaking vs. Breaking)		Percent Relative Change in Terminal Dimensionless Velocity (%)	Percent Relative Change in Rate of Damping (%)
Impermeable	Dry	SP5 vs. SP13	Inlet Sphere	46,14	0,00
			Outlet Sphere	45,31	0,00
Impermeable	Half-Water	SP7 vs. SP15	Inlet Sphere	-11,64	63,64
			Outlet Sphere	-22,20	129,41
Porous	Dry	SP6 vs. SP14	Inlet Sphere	85,14	0,00
			Outlet Sphere	69,87	45,45
Porous	Half-Water	SP8 vs. SP16	Inlet Sphere	-11,31	28,57
			Outlet Sphere	-27,57	52,00

NA*= As the divider in the equation is zero, comparison is not applicable.

5.1 Comparison of Impermeable and Porous Bottom Cases

The ranges of the deviation along the Y-axis in Table 5.1 and Table 5.2 indicate that regardless from the other experimental conditions, the range of the deviation along the Y-axis for the cases with the porous bottom is wider than the range of the deviation along the Y-axis for the cases with the impermeable bottom. Therefore, it can be understood that the motion of the spheres is significantly affected by the irregular surface of the porous bottom.

The permeability of the bottom mostly affected the energy of the solitary wave, which created the driving force for the motion of the spheres. Therefore, the impermeable and porous cases are compared to investigate the effect of the bottom permeability on the terminal dimensionless velocity and rate of damping. Some portion of the initial energy of the solitary wave is dissipated more on the porous bottom than the impermeable bottom. So, after the first impact of the solitary wave, the terminal dimensionless velocities of the spheres moving on the impermeable bottom became higher than the terminal dimensionless velocities of the spheres moving on the porous bottom. This difference can also be seen from the Table 5.3 that the terminal dimensionless velocities of the spheres moving on the impermeable bottom were around 10% to 63% higher than the terminal dimensionless velocities of the spheres moving on the porous bottom.

The increased permeability of the bottom creates a friction drag on the flow of the solitary wave. Therefore, in Table 5.1 and Table 5.2, it can be seen that all of the rate of damping values for the cases on the porous bottom are negative that indicates the spheres were losing velocity while they are moving on the porous bottom. On the contrary, the rate of damping values for the cases on the impermeable bottom were changing as positive or negative depends on the water level change as dry or half-water. However, from the comparison of the rate of damping values between the cases on the impermeable and porous bottom, it can be concluded that the damping along the horizontal area is much higher on the porous bottom than the damping on the impermeable bottom. This difference can also be seen from the Table 5.3 that the rate of damping values of the spheres moving on the impermeable bottom were around 2% to 125% lower than the rate of damping values of the spheres moving on the porous bottom.

5.2 Comparison of Dry and Half-Water Cases

The dry and half-water cases have no relation considering the ranges of deviations of the spheres along the Y-axis presented in Table 5.1 and 5.2.

The terminal dimensionless velocities of the spheres were generally higher for the spheres in dry condition than the spheres in half-water condition except for the double sphere cases under the effect of the breaking solitary waves. These differences can also be seen from the Table 5.4 that generally, the terminal dimensionless velocities of the spheres in dry condition were around 13% to 45% higher than the terminal dimensionless velocities of the spheres in half-water condition, contrarily, in the double sphere cases, the terminal dimensionless velocities of the spheres under the attack of breaking solitary waves in dry condition were around 15% to 48% lower than the terminal dimensionless velocities of the spheres under the attack of breaking solitary waves in half-water condition. The spheres in Case 15 and Case 16 are marked as an exception as the spheres in these cases did not collide. In these exceptional cases, the terminal dimensionless velocities of the spheres in half-water condition were greater than the terminal dimensionless velocities of the spheres in dry condition. The reasons behind this unusual behavior are discussed in detail in Section 5.4.

The rate of damping values were increased in magnitude with increased friction force due to the presence of the water body. The spheres were slowed down while they were moving on the horizontal area as the damping force on the sphere was increased due to the water level increase from dry condition to the half-water condition. Therefore, from the results and the observations on the dry and half-water cases, the damping of the spheres moving in the half-water condition was higher than the damping of the spheres moving in the dry condition. This difference can also be seen from the Table 5.4 that the rate of damping values of the spheres in the dry condition were around 56% to 112% lower than the rate of damping values of the spheres in the half-water condition.

5.3 Comparison of Breaking and Non-Breaking Solitary Wave Cases

The type of the solitary wave as breaking and non-breaking has no significant effect on the deviation along the Y-axis and the rate of damping, as can be seen from Table 5.1 and Table 5.2. On the other hand, it can be seen from Table 5.1, Table 5.2 and Table 5.5 that the type of solitary wave was affecting the terminal dimensionless velocities of the spheres, significantly.

The solitary waves lose most of their energy on the breaking process. As the solitary waves were climbing up from the slope, the breaking solitary waves were broken before the spheres; on the contrary, the non-breaking solitary waves were passed the spheres without breaking process. Therefore, the terminal dimensionless velocities of the spheres under the attack of non-breaking solitary waves are higher than the spheres under the attack of breaking solitary waves except for Case 15 and Case 16. These differences can also be seen from the Table 5.5 that generally, the terminal dimensionless velocities of the spheres under the attack of non-breaking solitary waves were around 12% to 86% higher than the terminal dimensionless velocities of the spheres under the attack of breaking solitary waves, contrarily, in the double sphere cases, the terminal dimensionless velocities of the spheres under the attack of non-breaking solitary waves in half-water condition were around 11% to 28% lower than the terminal dimensionless velocities of the spheres under the attack of breaking solitary waves in half-water condition. Spheres in these exceptional cases did not collide, and this situation creates an exception that the terminal dimensionless velocities of the spheres under the attack of breaking solitary waves are higher than the terminal dimensionless velocities of the spheres under the attack of non-breaking solitary waves. The reasons behind this exceptional behavior are discussed in detail in Section 5.4.

5.4 Assessment of Collision Behavior

The analysis of the motion of the spheres was extended for the double spheres because while the single spheres were only moving on the horizontal area, the double spheres as named as “inlet sphere” and “outlet sphere” were moving with the collision on the horizontal area at most of the cases. Therefore, the assessment of the collision behavior of the spheres is carried out in this section for double sphere cases. The assessment was carried out considering the change in the distance between the center of the spheres while they were moving on the horizontal area. Therefore, figures representing the change in the distance between the center of the spheres with respect to the dimensionless trajectory along the X-axis (X/D) were prepared. These figures consist of three types of lines similar to the figures presenting experimental results (Figures 4.6-4.21), indicating each of 21 repetitions (grey lines), the mean line of the repetitions (black line) and 95% confidence bands (red lines). The black and red lines are given up to a selected X/D value due to the same reasons stated in Section 4.3.

The non-dimensional distance between the center of the spheres should be equal to 1 if the collision is nearly elastic collision without any deformation. However, even the spheres used in the present experiments collided almost elastically, which indicates that the minimum distance between the center of the spheres should be equal to 1; due to the accuracy level of the image processing algorithm mentioned in Section 3.5, there might be slight deviations from this condition up to 0.08 (corresponding to 8 mm). The discussions are given based on examples for each of the comparison categories, namely impermeable/porous bottom, dry/half-water level and non-breaking/breaking solitary waves; however, these discussions hold for all the cases in its comparison category.

As stated in Section 5.1, the dimensionless velocities of the spheres were higher on the impermeable bottom than on the porous bottom. The effect of the impermeable and porous bottom in the behavior of the spheres considering the changes in the distance between the centers of the spheres with respect to X/D is given for Case 5 (SP5-NB-T-DI) and Case 6 (SP6-NB-T-DP) in Figure 5.1a and Figure 5.1b, respectively. The initial distance decrease between the centers of the spheres due to the solitary wave attack was faster on the impermeable bottom than the porous bottom. In other words, the distance traveled before the collision of the spheres was lower on the impermeable bottom than the porous bottom. The ranges of deviation along the Y-axis presented in Table 5.2 is wider for the spheres moving on the porous bottom due to the irregularities of this region. This situation significantly affected the distance between the center of the spheres on the porous cases, especially after the collision of the spheres. In Figure 5.1b, it can be observed that the distance between the center of the spheres oscillated significantly after the collision of the spheres. However, the change in the distance between the center of the spheres along the X-axis was smaller compared to the change in the distance between the center of the spheres along the Y-axis. Therefore, the assessment of the collision behavior was conducted until the collision of the spheres for the comparison of the impermeable and porous cases.

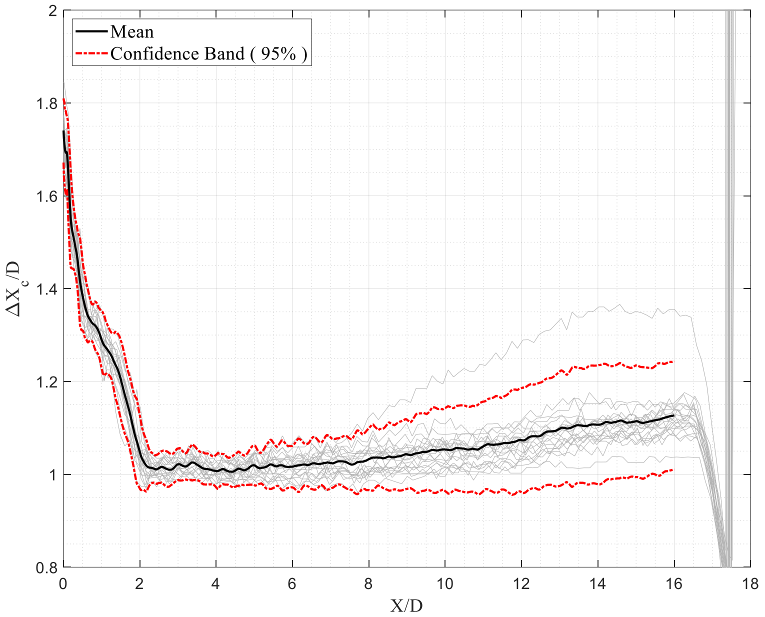

(a, SP5-NB-T-DI: Two Spheres under Non-Breaking Wave Attack on the Impermeable Slope and Impermeable Horizontal Area for Dry Condition)

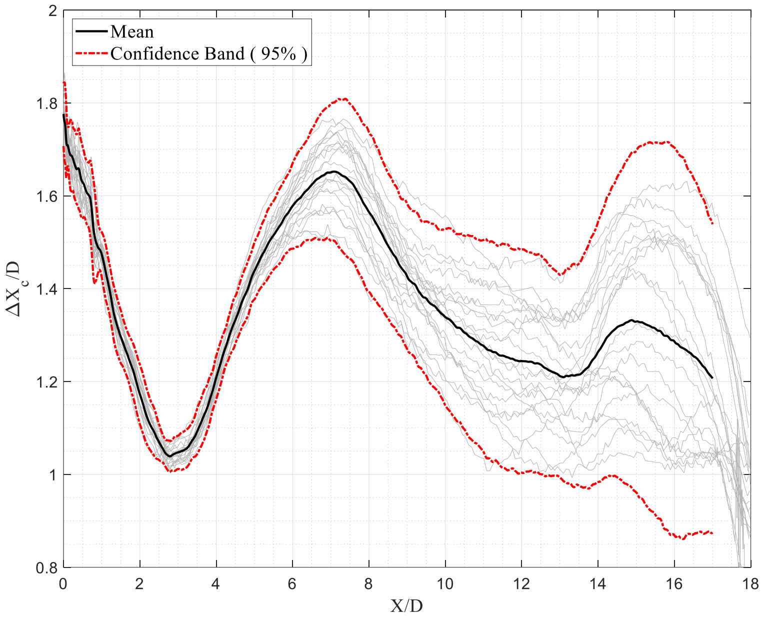

(b, SP6-NB-T-DP: Two Spheres under Non-Breaking Wave Attack on the Porous Slope and Porous Horizontal Area for Dry Condition)

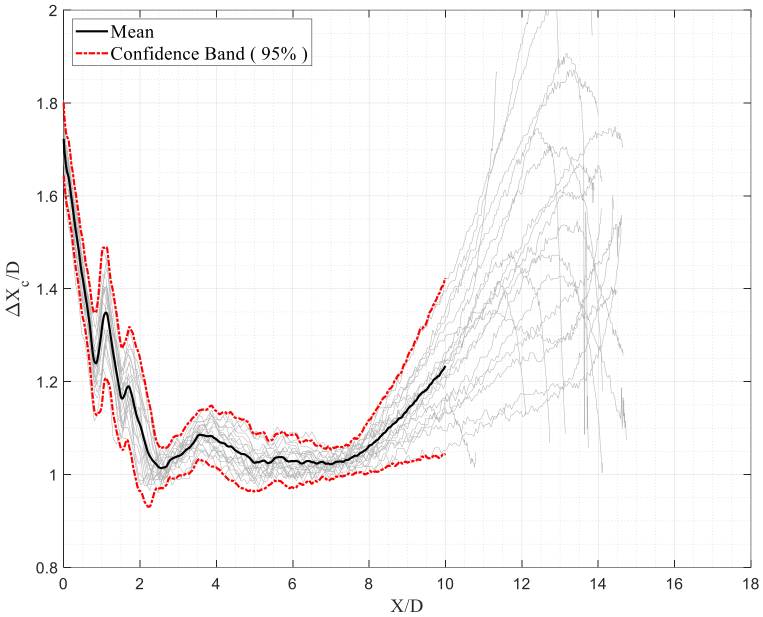

(c, SP7-NB-T-HI: Two Spheres under Non-Breaking Wave Attack on the Impermeable Slope and Impermeable Horizontal Area for Half-Water Condition)

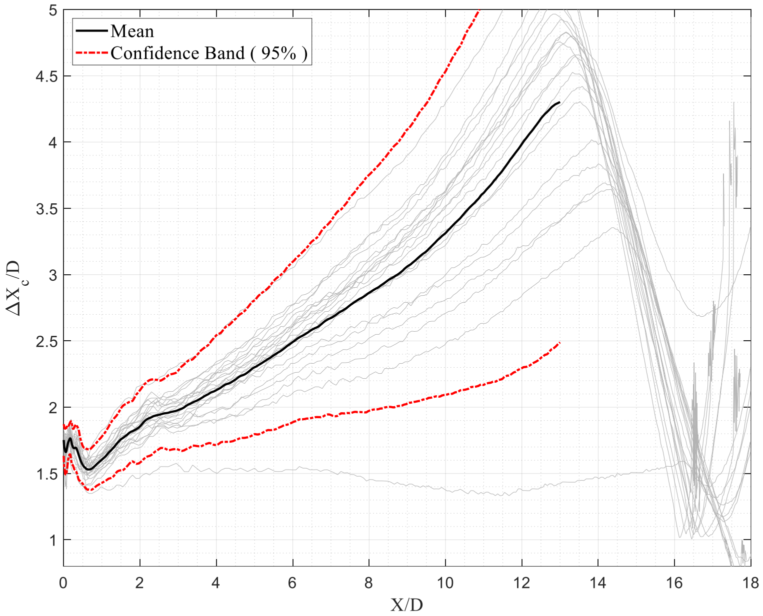

(d, SP15-B-T-HI: Two Spheres under Breaking Wave Attack on the Impermeable Slope and Impermeable Horizontal Area for Half-Water Condition)

Figure 5.1: Non-Dimensional Distance Between the Centers of the Spheres (a) Impermeable Bottom with Dry Condition (b) Porous Bottom with Dry Condition (c) Impermeable Bottom with Half-Water Condition (d) Impermeable Bottom with Half-Water Condition under the Attack of Breaking Solitary Wave

The effect of the water level change on the behavior of the collision of the spheres were examined with the selected sample cases Case 5 (SP5-NB-T-DI) and Case 7 (SP7-NB-T-HI). The change in the distances between the centers of the spheres with respect to X/D is given in Figure 5.1a and Figure 5.1c for Case 5 (dry case) and Case 7 (half-water case), respectively. The decrease rate of the distance between the center of the spheres for dry condition changes at a location nearly half of the distance required for the collision and becomes milder. The example of this mentioned change can be seen in Figure 5.1a for Case 5 that the decrease rate of the distance between the center of the spheres became milder around X/D=0.75. The reason behind this change was examined using different video recordings related to the given condition and discussed based on the snapshot from an experiment in the group of Case 5 presented in Figure 5.2a. In this figure, it can be seen that the inlet sphere blocks the solitary wave on the first impact; as a result, the water body could not fill the gap between the spheres in that period. Therefore, while the solitary wave pushed the inlet sphere significantly, the outlet sphere stayed at rest due to this block that the solitary wave could not get a chance to push the outlet sphere. But, after this gap was filled with the water body, the solitary wave got a chance to interact with the outlet sphere and pushed the outlet sphere significantly; as a result of this, the rate of decrease of the distance between the spheres became milder. On the other hand, the solitary wave interacted with the inlet and outlet spheres in the half-water condition similarly, and the spheres were pushed by the first impact of the solitary wave almost at the same time. However, the decrease rate of the distance between the spheres in the half-water condition oscillated in the region where the distance between the centers of the spheres is decreasing. In Figure 5.1c, an example of the mentioned significant oscillations on the decrease of the distance between the center of the spheres can be seen until X/D=2.5. The solitary waves in the half-water condition could create strong vortices while they were passing on the spheres due to the water body that surrounded the spheres before the solitary wave attack. The generated vortices around the spheres due to the solitary wave attack were captured, and an example of mentioned vortices is given in Figure 5.2b. These vortices influenced the trajectories as well as the velocities of the spheres, significantly. Except for the spheres in Case 15 and Case 16, all of the spheres in double sphere cases collided almost elastically; therefore, there was a slight increase in the distances between the center of the spheres just after the collision. However, this small gap between the spheres was closed rapidly as the inlet sphere was pushed more than the outlet sphere by the solitary wave flow. After the collision of the spheres, while the spheres in the dry condition moved together almost at the end of the horizontal area, the spheres in the half-water condition moved together for a shorter distance than divided from each other. The damping of the flow, as well as the vortices generated around the moving spheres in half-water condition, influenced the trajectories and the velocities of the spheres considerably.

The non-breaking and the breaking solitary wave cases were also examined on their effect on the collision behavior. From the comparison of the cases, the most important observation can be stated that the spheres did not collide in the breaking cases at the half-water level, as mentioned before (Case 15 and Case 16). Although the distance between the center of the spheres was decreasing slightly at the beginning of the motion of the spheres, this distance was continuously increased until the end of the horizontal area. The example of the mentioned distance change between the center of the spheres is shown in Figure 5.1d for Case 15. As can be seen from the Figure 5.2c, the solitary wave was breaking approximately in between the inlet and the outlet spheres; therefore, the outlet sphere was taken away towards the end of the horizontal area by the breaking solitary wave and increased its dimensionless velocity, while the inlet sphere was influenced by the breaking solitary wave slightly and moved with a relatively small dimensionless velocity compared with the outlet sphere.

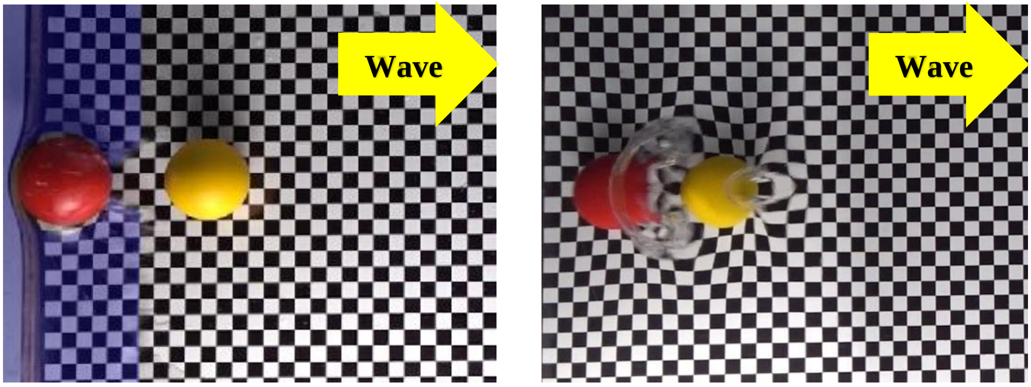

(a, SP5-NB-T-DI: Two Spheres under Non-Breaking Wave Attack on the Impermeable Slope and Impermeable Horizontal Area for Dry Condition, Non-Breaking Solitary Wave is Colored)

(b, SP7-NB-T-HI: Two Spheres under Non-Breaking Wave Attack on the Impermeable Slope and Impermeable Horizontal Area for Half-Water Condition)

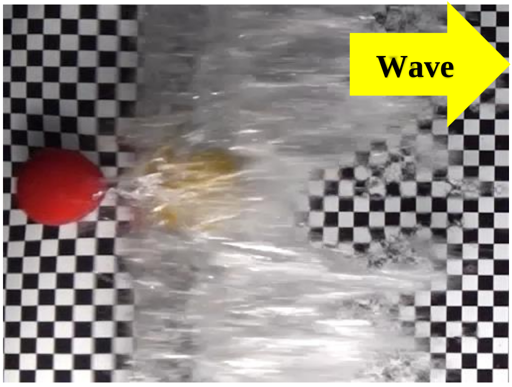

(c, SP15-B-T-HI: Two Spheres under Breaking Wave Attack on the Impermeable Slope and Impermeable Horizontal Area for Half-Water Condition)

Figure 5.2: Snapshots from the Experiments for the Collision Discussions

CHAPTER 6

CONCLUSIONS

In this study, the motion and collision of the spheres under solitary wave attack are investigated, and a unique integrated dataset on the motion and collision of the spheres under solitary wave attack is presented. In the physical model experiments, the effect of changing bottom permeability, water level and type of the solitary wave on the motion of a single sphere and double sphere under solitary wave attack is investigated. All of these changes created 16 different experimental cases on 4 different experimental setups. The results are discussed mainly based on the effect of the mentioned change of the parameters. Additionally, the collision behavior of the spheres in double sphere cases is investigated to better understand the behavior of the spheres under a solitary wave attack. Although there are studies that examined the motion of the spherical particles under certain flow conditions mentioned in Chapter 2, this study is the first study that examines the motion and collision of the spherical particles under the attack of solitary waves.

Based on the results and discussions on the experimental results, the following main conclusions are summarized:

- The damping applied by the porous bottom is higher than the damping applied by the impermeable bottom (From Table 5.3, around 2% to 125% less damping on the impermeable bottom than porous bottom considering the rate of damping values). Besides, the irregularities on the porous bottom significantly affected the trajectories of the spheres. Therefore, the deviation along the Y-axis was wider in porous cases than impermeable cases.
- The water level change from 30 cm to 35 cm does not have a significant effect on the deviation along Y-axis. However, the friction force applied by the water body and the effect of the vortices created by the interaction of the

waves and moving spheres became more significant with the increased water level (From Table 5.4, around 56% to 112% less damping in dry condition than half-water condition considering the rate of damping values). Therefore, the characteristics of the motion of the spheres are changed in both the speeding-up region up to the terminal dimensionless velocity point and the slowing down region.

- In the present study, the breaking solitary waves lost their energy at the beginning of the horizontal area. In contrast, the non-breaking solitary waves were able to proceed without breaking. Therefore, the terminal dimensionless velocity of the spheres, for all the single sphere cases and the double sphere cases where the spheres collided, is found to be higher (around 12% to 86% higher from the comparison of terminal dimensionless velocities in Table 5.5) in the non-breaking solitary wave cases compared to the breaking solitary wave cases.
- The collision behavior of the spheres is changed depending on the type of solitary wave as non-breaking or breaking and water level as 30 cm and 35 cm. Except for the spheres affected by the breaking solitary waves in half-water condition, all of the spheres in double sphere cases collided with each other. The results showed that the permeability of the bottom condition does not have a significant contribution to the collision behavior.

Overall, the fundamentals of the motion and collision of the spheres under a solitary wave attack on a horizontal region are described. The CFD solvers, coupled with the DEM solvers, gained popularity for coastal and ocean engineering applications in recent years. Therefore, the unique dataset presented in this study can also be used in these CFD applications for calibration and validation purposes. On the other hand, the major drawbacks of the present study should be addressed for future studies. Two significant drawbacks of the present study are discussed below:

i) The velocity field around the spheres should be measured in detail to be able to discuss further the hydrodynamic forces that affected the motion of the spheres. Therefore, an appropriate measuring system has to be considered for future studies.

ii) The irregularities in the porous region distracted the trajectories of the spheres, and the bias on the data is increased due to these unexpected trajectories. Therefore, the porous region should be constructed such that the possible irregularities in the porous region are avoided.

REFERENCES

Belov, A. G., 2019. “Calculation of Confidence Bands for the Mean of Repeated Observations. Computational Mathematics and Modeling”, 30(3), 285–294.

Brilliantov, N., & Pöschel, T., 1999. “Rolling as a ‘continuing collision’”, The European Physical Journal B, 12(2), 299-301.

Gondret, P., Lance, M., Petit, L., 2002. “Bouncing Motion of Spherical Particles in Fluids”, Physics of Fluids”, 14, 643-652.

Goring, D. G., 1979. “Tsunamis – The Propagation of Long Waves onto Shelf”, PhD Dissertation, California Institute of Technology, Pasedane, California, USA.

Goseberg, N., Nistor, I., Mikami, T., Shibayama, T., Stolle, J., 2016. “Nonintrusive SpatiotemporalSmart DebrisTracking in Turbulent Flows with Application to Debris-Laden Tsunami Inundation”, Journal of Hydraulic Engineering,142(12), 04016058.

Grilli, S. T., Svendsen, I. A., Subramanya, R., 1997. “Breaking Criterion and Characteristics for Solitary Waves on Slopes”. Journal of Waterway, Port, Coastal, and Ocean Engineering,102-112.

Guler, H.G., Arikawa, T., Baykal, C., Goral, K.D., Yalciner, A.C., 2018. “Motion of Solid Spheres under Solitary Wave Attack: Physical and Numerical Modeling”, in proceedings of International Conference on Coastal Engineering (ICCE) 2018, ASCE.

Imamura, F., Goto, K., Ohkubo, S., 2008. “A numerical model for the transport of a boulder by tsunami”. Journal of Geophysical Research, 113(C1).

Jarque, C.M., 2011. “Jarque-Bera Test”, in Lovric M. (eds) International Encyclopedia of Statistical Science, Springer, Berlin, Heidelberg.

Jensen, B., Christensen, E. D., Sumer, B. M., & Vistisen, M., 2015. “Flow and Turbulence at Rubble-Mound Breakwater Armor Layers under Solitary Wave”. Journal of Waterway, Port, Coastal, and Ocean Engineering, 141(6), 04015006.

Joseph, G., Zenit, R., Hunt, M., Rosenwinkel, A., 2001. “Particle Wall Collisions in A Viscous Fluid”, Journal of Fluid Mechanics, 433, 329-346.

Luetkepohl, H., Staszewska-Bystrova, A., Winker, P., 2013. “Comparison of Methods for Constructing Joint Confidence Bands for Impulse Response Functions”. SSRN Electronic Journal.

Malek-Mohammadi, S., & Testik, F. Y., 2010. “New Methodology for Laboratory Generation of Solitary Waves”. Journal of Waterway, Port, Coastal, and Ocean Engineering, 136(5), 286-294.

Nistor, I., Goseberg, N., Stolle, J., 2017. “Tsunami-Driven Debris Motion and Loads: A Critical Review”, Frontiers in Built Environment, 3.

Pitois, O., Moucheront, P., Chateau, X., 2000. “Liquid Bridge between Two Moving Spheres: An Experimental Study of Viscosity Effects”. Journal of Colloid and Interface Science, 231(1), 26–31.

Rueben, M., Cox, D., Holman, R., Shin, S., Stanley, J., 2015. “Optical Measurements of Tsunami Inundation and Debris Movement in a Large-Scale Wave Basin”, Journal of Waterway, Port, Coastal, and Ocean Engineering,141(1), 04014029.

Schloz, F., 2008. “Applications of the Non-Central t-Distribution”, Washington University STAT 498B Lecture Notes, Accessed from http://faculty.washington.edu/fscholz/DATAFILES498B2008/NoncentralT.pdf.

Shafiei, S., Melville, B. W., Shamseldin, A. Y., Beskhyroun, S., Adams, K. N., 2016. "Measurements of tsunami-borne debris impact on structures using an embedded accelerometer". Journal of Hydraulic Research,54(4), 435-449.

Stolle, J., Goseberg, N., Nistor, I., Petriu, E., 2017. "Probabilistic Investigation and Risk Assessment of Debris Transport in Extreme Hydrodynamic Conditions", Journal of Waterway, Port, Coastal, and Ocean Engineering, 144(1), 04017039.

Stolle, J., Nistor, I., Goseberg, N., 2016. "Optical Tracking of Floating Shipping Containers in a High-Velocity Flow". Coastal Engineering Journal,58(2).

Stolle, J., Takabatake, T., Hamano, G., Ishii, H., Iimura, K., Shibayama, T., . . . Petriu, E., 2019. "Debris Transport over a Sloped Surface in Tsunami-Like Flow Conditions", Coastal Engineering Journal, 1-15.

Witters, J., & Duymelinck, D., 1986. "Rolling and sliding resistive forces on balls moving on a flat surface", American Journal of Physics, 54(1), 80-83.

Zama, S., Nishi, H., Hatayama, K., Yamada, M., Yoshihara, H., Ogawa, Y., 2012. "On Damage of Oil Storage Tanks due to the 2011 off the Pacific Coast of Tohoku Earthquake (Mw9.0), Japan".

Zhang, Y., & Yang, L., 2017. "A smooth simultaneous confidence band for correlation curve". Test, 27(2), 247–269.